2019

SCATTERING STATISTICS OF A NEGATIVELY BUOYANT THERMAL PLUME

Forge, Timothy

Monterey, CA; Naval Postgraduate School

NAVAL POSTGRADUATE SCHOOL

MONTEREY, CALIFORNIA

THESIS

SCATTERING STATISTICS OF A NEGATIVELY BUOYANT THERMAL PLUME

by

Timothy Forge

June 2019

Thesis Advisor:	Derek Olson
Second Reader:	John A. Colosi

THIS PAGE INTENTIONALLY LEFT BLANK

REPORT DOCUMENTATION PAGE			*Form Approved OMB No. 0704-0188*

1. AGENCY USE ONLY *(Leave blank)*	**2. REPORT DATE** June 2019	**3. REPORT TYPE AND DATES COVERED** Master's thesis

4. TITLE AND SUBTITLE
SCATTERING STATISTICS OF A NEGATIVELY BUOYANT THERMAL PLUME

5. FUNDING NUMBERS

6. AUTHOR(S) Timothy Forge

7. PERFORMING ORGANIZATION NAME(S) AND ADDRESS(ES)
Naval Postgraduate School
Monterey, CA 93943-5000

8. PERFORMING ORGANIZATION REPORT NUMBER

9. SPONSORING / MONITORING AGENCY NAME(S) AND ADDRESS(ES)
N/A

10. SPONSORING / MONITORING AGENCY REPORT NUMBER

11. SUPPLEMENTARY NOTES The views expressed in this thesis are those of the author and do not reflect the official policy or position of the Department of Defense or the U.S. Government.

12a. DISTRIBUTION / AVAILABILITY STATEMENT
Approved for public release. Distribution is unlimited.

12b. DISTRIBUTION CODE
A

13. ABSTRACT (maximum 200 words)

Reverberation often limits effectiveness of active sonar systems due to the difficulty in discriminating between a desired target and the undesired echo returns scattered from inhomogeneities in the water column and its boundaries. An understanding of the background environment that produces the reverberation is essential for optimization of sonar systems, as it will assist in the reduction of clutter, and may also allow active systems to remotely classify the reverberation source.

Many studies have dealt with the scattering properties of the boundaries and volume of the water column; however, little attention has been paid to the statistical characterization of volume scattering due to turbulence. In this thesis, laboratory measurements of high-frequency (70kHz, 120kHz, and 200kHz) narrowband acoustic backscattering through a negatively buoyant thermal plume have been performed, and the empirical echo distributions matched to statistical functions. Results show that the reverberation statistics did not always follow a Rayleigh probability distribution function (PDF), but exhibited sub-Rayleigh behavior with lighter tails, aligning more closely to a Rician PDF. A qualitative assessment of these results infers that there is a weak coherent component of the reverberation due to the temperature stratification of the thermal plume, and a strong incoherent component due to the turbulent mixing.

14. SUBJECT TERMS
turbulent plume, echo backscatter statistics, high frequency, reverberation, scattering, volume scattering

15. NUMBER OF PAGES
83

16. PRICE CODE

17. SECURITY CLASSIFICATION OF REPORT	**18. SECURITY CLASSIFICATION OF THIS PAGE**	**19. SECURITY CLASSIFICATION OF ABSTRACT**	**20. LIMITATION OF ABSTRACT**
Unclassified	Unclassified	Unclassified	UU

NSN 7540-01-280-5500

Standard Form 298 (Rev. 2-89)
Prescribed by ANSI Std. 239-18

THIS PAGE INTENTIONALLY LEFT BLANK

Approved for public release. Distribution is unlimited.

SCATTERING STATISTICS OF A NEGATIVELY BUOYANT THERMAL PLUME

Timothy Forge
Lieutenant, Royal Australian Navy
BS, University of Melbourne, 2006

Submitted in partial fulfillment of the
requirements for the degree of

MASTER OF SCIENCE IN PHYSICAL OCEANOGRAPHY

from the

NAVAL POSTGRADUATE SCHOOL
June 2019

Approved by: Derek Olson
Advisor

John A. Colosi
Second Reader

Peter C. Chu
Chair, Department of Oceanography

THIS PAGE INTENTIONALLY LEFT BLANK

ABSTRACT

Reverberation often limits effectiveness of active sonar systems due to the difficulty in discriminating between a desired target and the undesired echo returns scattered from inhomogeneities in the water column and its boundaries. An understanding of the background environment that produces the reverberation is essential for optimization of sonar systems, as it will assist in the reduction of clutter, and may also allow active systems to remotely classify the reverberation source.

Many studies have dealt with the scattering properties of the boundaries and volume of the water column; however, little attention has been paid to the statistical characterization of volume scattering due to turbulence. In this thesis, laboratory measurements of high-frequency (70kHz, 120kHz, and 200kHz) narrowband acoustic backscattering through a negatively buoyant thermal plume have been performed, and the empirical echo distributions matched to statistical functions. Results show that the reverberation statistics did not always follow a Rayleigh probability distribution function (PDF), but exhibited sub-Rayleigh behavior with lighter tails, aligning more closely to a Rician PDF. A qualitative assessment of these results infers that there is a weak coherent component of the reverberation due to the temperature stratification of the thermal plume, and a strong incoherent component due to the turbulent mixing.

THIS PAGE INTENTIONALLY LEFT BLANK

TABLE OF CONTENTS

LIST OF FIGURES

LIST OF TABLES

THIS PAGE INTENTIONALLY LEFT BLANK

ACKNOWLEDGMENTS

Firstly, thank you to my thesis advisor, Derek Olson. I would never have gotten this far without all of your help, support and suggestions. My second reader, John Colosi, thank you very much for passing a critical eye through my work, and for helping me to finally complete it. To all the faculty and teaching staff, I am greatly indebted to you. I have learned so much throughout my time here and cannot thank you enough. To my original cohort (Alana, Jen, Kevin, Ash, Terrence, Jeremy, Vinny and Roz) thank you for all your help along the way, particularly the study sessions in the first two quarters where the learning curve was the toughest.

Finally, thank you to my wife, Helen, and son, Luke, for your support and love throughout the last 18 months, and for reminding me that I still have a life outside of NPS.

THIS PAGE INTENTIONALLY LEFT BLANK

I. INTRODUCTION

At the most fundamental level, active echo location (or sonar) uses short pulses of sound to determine the distance between a sound source and a target. The two-way acoustic travel time t, yields the distance d, via the equation

$$d = c_0 t \tag{1}$$

where c_0 is the mean speed of sound between the source and the target. However, the sea is not a homogenous body, and there are many factors that complicate what is otherwise a very straightforward concept. Variations in temperature, salinity and density change the speed at which sound propagates, resulting in differences in the arrival time back to the receiver. Refraction and reflection effects within the water column allow for sound to travel along multiple different paths between the source and target or target and receiver. Absorption of the sound energy from the seawater itself can weaken the return signal intensity. Background noise from other sources can make the target indistinguishable from its surroundings. Then there is the presence of inhomogeneities or scatterers within the water column, and on its boundaries, which act to distort an initial sharp sound pulse (Talley et al. 2011, Colosi 2016). These scatterers can range from fish, plankton, and other biological sources, to roughness at the top and bottom surfaces or boundaries. The result of the presence of these scatterers is the formation of discontinuities or continuous variation in the physical properties of the medium. As acoustic energy passes through this non-uniform medium, a portion of the energy is intercepted and reradiated by the scatterers (Urick 2010). This reradiation or scattering of acoustic energy often results in an undesired signal at the receiver that mimics a target, often obscuring the desired target echo (Burdic 1991); we refer to this as reverberation.

There are three classes of reverberation producing scatterers in the sea. Those that reradiate sound energy from within the volume, or body, of the sea (primarily biological, particulate matter or sound speed variations in the water column) result in what we refer to as volume reverberation. Reverberation that results from interactions with the sea surface or sea floor is often analytically considered together and collectively referred to as surface

reverberation. Furthermore, reverberation can be categorized as either continuous or discrete (Fialkowski 2010). Continuous reverberation is an incoherent quantity. It is comprised of mixed, indistinguishable echoes, sourced from reflections off closely spaced scatterers. Discrete reverberation can be a coherent or incoherent quantity and refers to strong, non-target echoes from localized scatterers (Fialkowski 2010).

A. STATISTICAL ANALYSIS OF ECHO BACKSCATTER

If reverberation is not properly dealt with through signal normalization and processing techniques it will often generate target false alarms. These false alarms (known as clutter) reduce the overall effectiveness of an active sonar system due to the difficulty in discriminating against real and false targets (Figure 1).

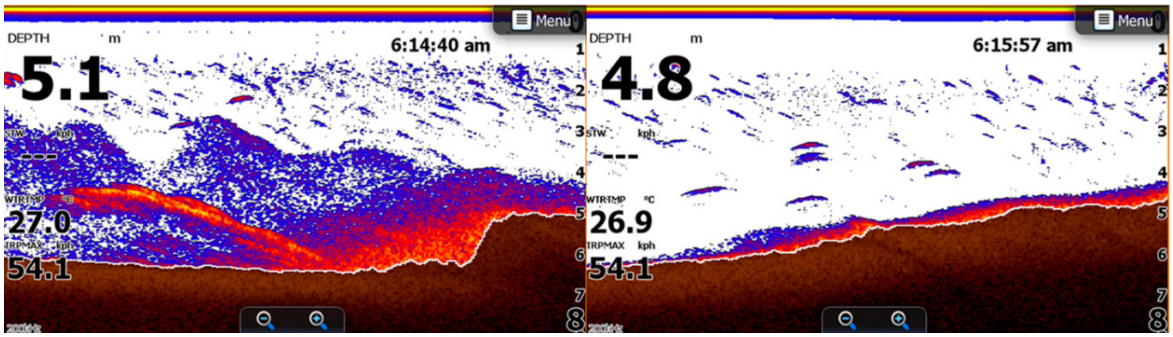

Figure 1. Cluttered and Decluttered Echo Sounder Display. Source: Lowrance, https://www.lowrance.com/.

One processing technique in particular that can help to reduce the false alarm rate is the use of statistical methods that reject echoes which can be identified as being due to non-target scattering. In general, when the number of scatterers present is large enough, the echo amplitude distribution tends towards that of the Rayleigh distribution (Lyons and Abraham 1999). As such, it is often reasonable to assume Rayleigh statistics as a decision strategy (Ainslie 2010). However, many scattering amplitude distributions exhibit non-Rayleigh behavior, which can result in higher than expected false alarms. Thus, in order to adequately deal with sources of non-Rayleigh reverberation we must first identify which statistical distribution they most closely follow. The added benefit of this statistical analysis

approach is that once the statistical distribution of a scatterer is known, the otherwise undesirable reverberation can be exploited and used as a remote sensing tool (Stanton and Clay 1986, Stanton et al. 2018). Significant work has been conducted in identifying and classifying the sources of non-Rayleigh scatterers over a range of different echo frequencies and bandwidths, both near and far-away. Typically, this work has focused on the statistics of volume scattering due to biological life, such studies have been able to classify individual fish and zooplankton (Stanton et al. 2004), patches of fish (Stanton and Chu 2010) and determine the numerical density of fish (Lee and Stanton 2016). The statistics of boundary and seafloor scattering have also been explored, ranging from smooth homogeneous seafloors (Stanic and Kennedy 1993) to seafloors of varying sediments and roughness (Lyons and Abraham, 1999) through to very rough or rocky seafloors (Olson et al. 2019).

In addition to boundaries, physical bodies and particles in the water column, it has also been shown that the turbulent motion of the ocean can be observed acoustically (Ross and Lueck 2003). However, the majority of research in this area has been in using acoustic backscatter techniques to probe the structure of turbulence (Oeschger and Goodman 1996; Lavery and Ross 2007; Lavery et al. 2013) rather than analyze the statistical distributions.

B. THESIS OUTLINE

This thesis comprises five chapters, with the body of work primarily concerned with the statistical distribution of volume reverberation due to turbulent, buoyant plume induced via a temperature differential in an experimental tank. In chapter two we will delve into the background of turbulent flow, as well as the characteristics of reverberation and statistical distributions. Chapter three will establish the context for the experiment, and the conditions under which the experiment was conducted. Chapter four will detail the results of the experiment, with a discussion to follow in chapter five. The thesis will conclude with chapter six.

THIS PAGE INTENTIONALLY LEFT BLANK

II. BACKGROUND

To initiate the turbulent flow for the purposes of studying the acoustic backscatter statistics we created a temperature differential within the tank, which in turn resulted in a density differential, causing the denser fluid to sink due to negative buoyancy. The rate at which the denser fluid sinks can be determined via the reduced gravity (g') equation

$$g' = \frac{g\Delta\rho}{\rho_0} \tag{2}$$

This method is expected to produce a result very similar to what we observe in nature in the form of plumes and thermals, albeit negatively buoyant.

A. PLUMES AND THERMALS

Plumes and thermals describe distinct structures of vertical motion that occur due to a density contrast between the source fluid and the environment (Turner 1969). They are ubiquitous within nature and can often be seen in the form of billowing clouds/rising smoke in the atmosphere, or black/white smokers/hydrothermal vents in the oceans (Figure 2).

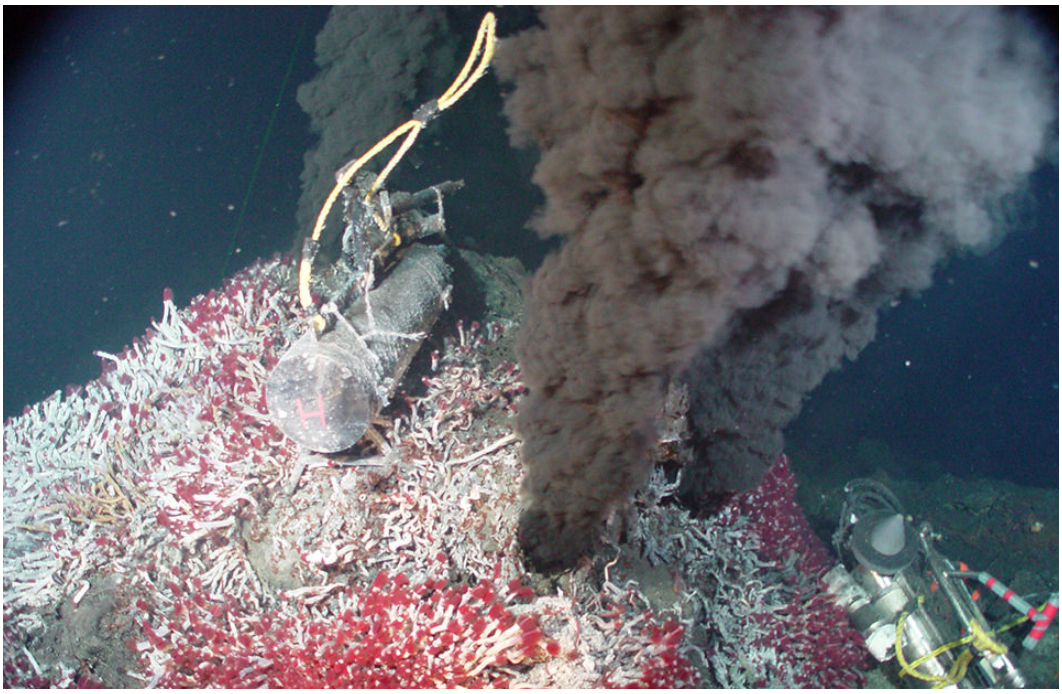

Figure 2. Hydrothermal Vent. Source: NOAA, https://oceanservice.noaa.gov.

Much like a jet, buoyant plumes are also observed to have a sharp boundary separating the rising (or sinking) turbulent fluid, and the quiescent surrounding environment (Turner 1969). As the plume transitions into the ambient environment it spreads out and widens. This is through the process of entrainment of the external fluid across its boundary by large eddies, which is then followed by smaller scale mixing of the external fluid towards the core (Turner 1969). This action mirrors that which is observed in a free jet and is illustrated in Figure 3.

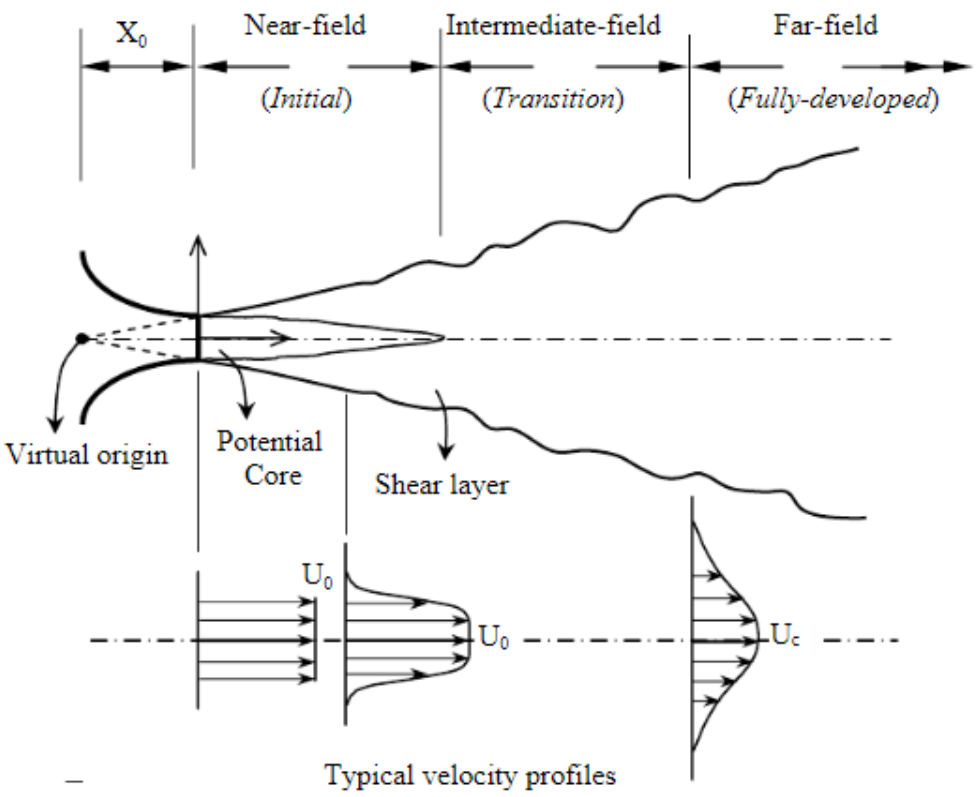

Figure 3. Schematic of a Free Turbulent Jet. Source: Abdel-Rahman (2010).

The free jet is often considered in three zones or fields, the near field (close to the source) is of interest to engineers for practical applications, as it has the greatest impact in influencing downstream conditions for heat, mass and momentum transfer. The intermediate field is the region of the flow where highly anisotropic turbulent structures grow and interact. The far field (distant from the source), also known as the self-similar region has received considerable attention from researchers as it is here that the turbulent flow is fully developed (Kolmogorov's locally isotropic assumption is valid) and the fine scales of turbulence can be interrogated (Ball et al. 2012).

B. TURBULENT FLOW

Turbulent flow involves erratic, chaotic or otherwise unpredictable fluctuations in the velocity field of a fluid. In the oceans it is the "*dominant physical process in the transfer*

of momentum and heat" (Thorpe 2007), and, in general, it is an extremely important topic in modern fluid dynamics as *"nearly all macroscopic flows we encounter within the natural world and in engineering practice are turbulent"* (Kundu et al. 2012). Through observation we can see that turbulent flow is comprised of many different scales of motion, from waves and bulges, through various sized eddies, until finally the turbulent structure is unresolvable (Figure 4).

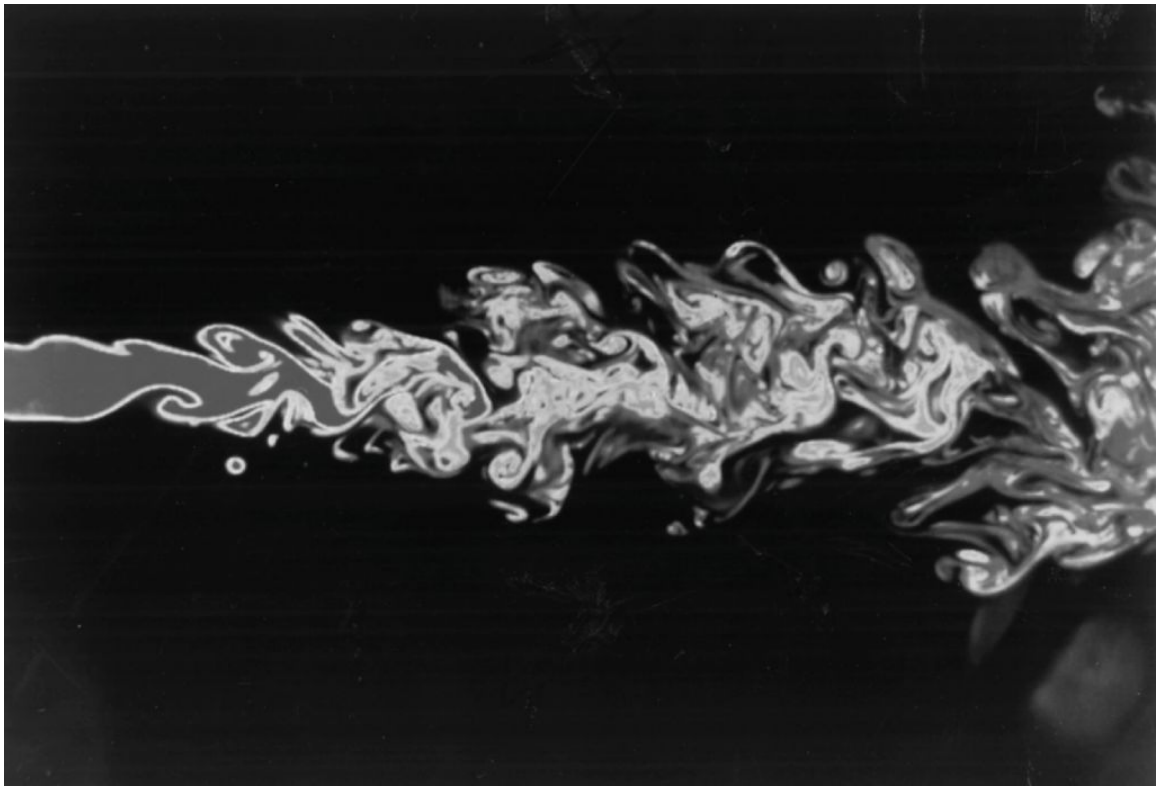

Figure 4. Turbulent Jet. Source: Prasad and Sreenivisan (1990).

Although the first systematic work on turbulence began with Osborne Reynold's in 1883 with his pipe flow experiments (Kundu et al. 2012), it was not until 1922 that Lewis Fry Richardson introduced the idea of the turbulent energy cascade. That is, turbulent kinetic energy enters the system at the largest scale of motion, it then breaks down due to instability, and is transferred to smaller and smaller scales before finally disappearing via

frictional conversion to thermal energy (Figure 5). This idea is central to the modern understanding of turbulence (Kundu et al. 2012).

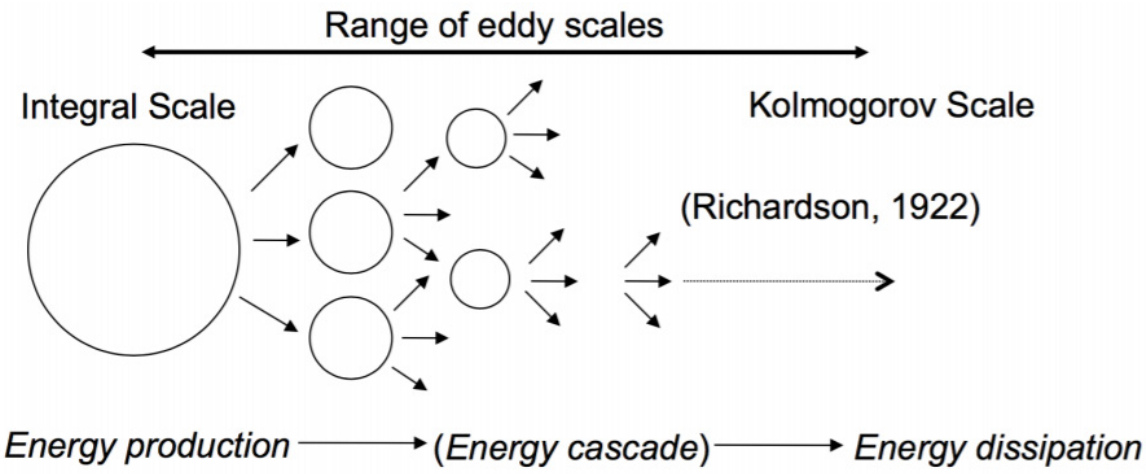

Figure 5. Richardson's Energy Cascade. Source: Gibbs (2016).

1. Kolmogorov Spectra

Richardson's insight was followed up on by the Russian mathematician Kolmogorov (1941), who, on the basis of three hypotheses and dimensional analysis, gave Richardson's ideas a quantitative shape (Kundu et al. 2012). His first two hypotheses were that, at small scales, turbulence is isotropic (equal in all directions) and only depends on two parameters, ν (viscosity, in units of m^2/s) and ε (dissipation, in units of m^2/s^3). Via dimensional analysis he derived that the smallest scales at which there is turbulent flow, or the scales at which energy begins to dissipate via viscosity (also known as the Kolmogorov scale) must be of size η, where

$$\eta = \left(\frac{\nu^3}{\varepsilon} \right)^{\frac{1}{4}} \tag{3}$$

Kolmogorov's third hypothesis was that at scales much smaller than ℓ (the largest eddy length scale) and much larger than η, there must exist an inertial subrange of eddy sizes, in which viscosity plays no role. That is, only the dissipation term ε, is important.

Again, via dimensional analysis, Kolmogorov derived that the energy spectrum within this inertial subrange must be proportional to

$$\varepsilon^{\frac{2}{3}} k^{\frac{-5}{3}} \tag{4}$$

where k is the wavenumber. This seminal work gave rise to the famous Kolmogorov five thirds law, which is highly regarded as "*one of the most important results of turbulence theory"* (Kundu et al. 2012). From this, we can express the energy within the inertial subrange as

$$E(k) = C\varepsilon^{\frac{2}{3}} k^{\frac{-5}{3}} \tag{5}$$

where C is a universal constant and $k \in [1/\ell, 1/\eta]$. From Kolmogorov's hypotheses, we can now take an energy distribution point of view to Richardson's idea of the energy cascade (Figure 6).

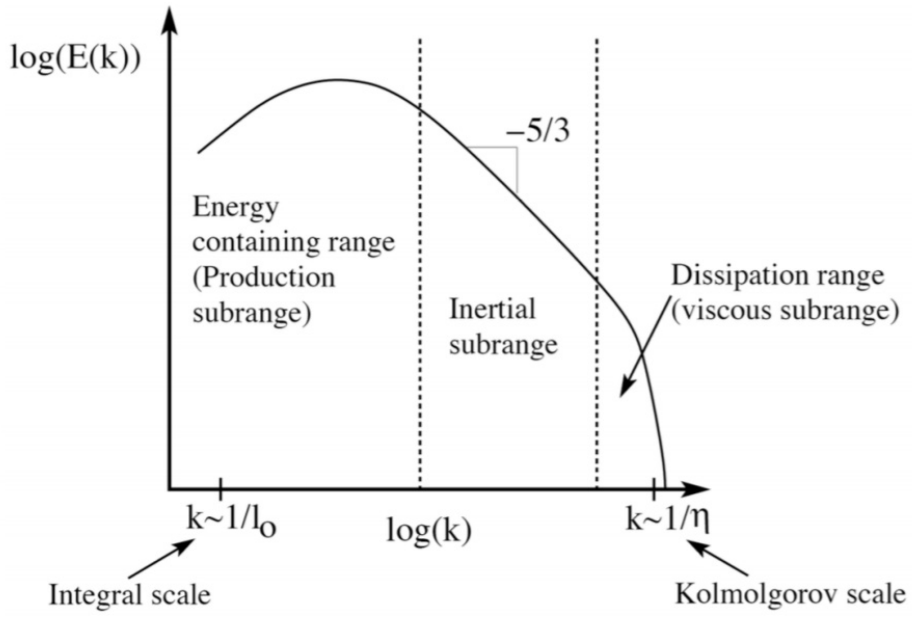

Figure 6. Turbulent Energy Spectra. Source: Gibbs (2016).

2. Reynolds Number

The Reynolds number (Re) is a dimensionless ratio used to characterize turbulent (or laminar) flow. It is named after Osborne Reynolds, whose work showed that flow in a pipe tends towards turbulence or irregularity when Re exceeds a certain value (Reynolds 1883). In general, Re is defined as

$$\mathrm{Re} = \frac{UL}{\nu} \tag{6}$$

where U and L are characteristic scales of the velocity and length of the flow, and ν is the kinematic viscosity of the fluid. From Reynolds' pipe flow experiment, it was shown that if Re is less than about 2300 the flow is laminar, and, if Re exceeds 4000 then the flow is turbulent (Pope 2000).

3. Reynolds Decomposition

In order to just examine the fluctuating or turbulent component of the flow, it is often necessary to separate the flow field $\mathbf{u}(x,t)$ into its constituent components of mean flow $\bar{\mathbf{u}}(x,t)$ and fluctuation from the mean $\mathbf{u}'(x,t)$, such that

$$\mathbf{u}(x,t) = \bar{\mathbf{u}}(x,t) + \mathbf{u}'(x,t) \tag{7}$$

This is known as the Reynolds decomposition (Kundu et al. 2012).

4. Taylor's Hypothesis

Taylor's Hypothesis (Taylor 1938), also known as the Frozen Turbulence Hypothesis, is a means of approximating spatial correlations from temporal correlations (Pope 2010). The assumption is that turbulent fluctuations at a single point are due to a frozen field of turbulence advected past that point (Kundu et al. 2012). In order to measure the spatial correlation of fluctuations an instantaneous observation of the entire field $\mathbf{u}(x)$ is required, often this is extremely difficult, or just not possible. A more simple and practicable technique is in the use of a single probe at a stationary point, this will measure a time series $\mathbf{u}(t)$ at that point. By assuming that the field of turbulence is frozen, and is being advected by the mean velocity $\bar{\mathbf{u}}$, we can say that the substitution

$$t \leftrightarrow \frac{x}{\mathbf{u}} \tag{8}$$

is valid. By doing this we are able to transform the time series $\mathbf{u}(t)$ into a spatial series $\mathbf{u}(x)$. However, the application of this approximation is limited with its accuracy linked to the ratio of turbulent velocity with mean velocity $\mathbf{u}_{rms} / \overline{\mathbf{u}}$. The approximation is considered quite accurate when $\mathbf{u}_{rms} / \overline{\mathbf{u}} \ll 1$, as this ratio increases the approximation will become less accurate, or fail altogether (Pope 2010).

C. ECHO BACKSCATTER CHARACTERISTICS

If we consider the echo strength of a single ping as an instantaneous measurement, we typically see a fluctuation from instant to instant in the strength of received echoes as measured by an active system (Stanton et al. 2018). These fluctuations can be due to a change in the position and phase relationship of the scatterers, or a change in number of scatterers through time (Urick 2010). We can begin to characterize the backscatter statistically by taking many samples and plotting the received echo magnitude against the frequency of occurrence, creating a probability distribution histogram (Figure 7).

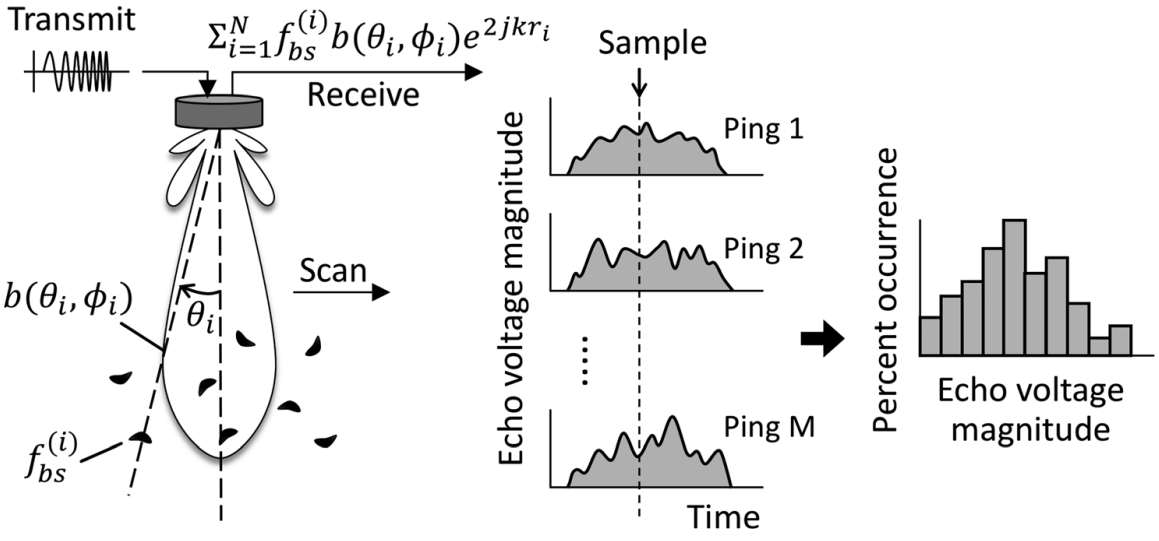

Figure 7. Echo Statistics Process. Source: Stanton et al. (2018).

The statistical behavior of echoes will vary greatly with the size, number and type of scatterers, as well as with the geometry and interference of the acoustic paths, and the presence of boundaries or discontinuities within the water column. The simplest case would involve a single scatterer (point scatterer) whose orientation does not change with time, direct path geometry, and a narrowband omni-directional sensor. For a series of echoes, it is expected that the probability distribution would be a spike at a distinct amplitude, as described by a delta function. If we now consider a slightly more realistic scenario where the scatterer is somewhat elongated (fishlike), and whose orientation and position does change with time, it is expected that the resultant probability distribution would be more spread out and complex (Figure 8).

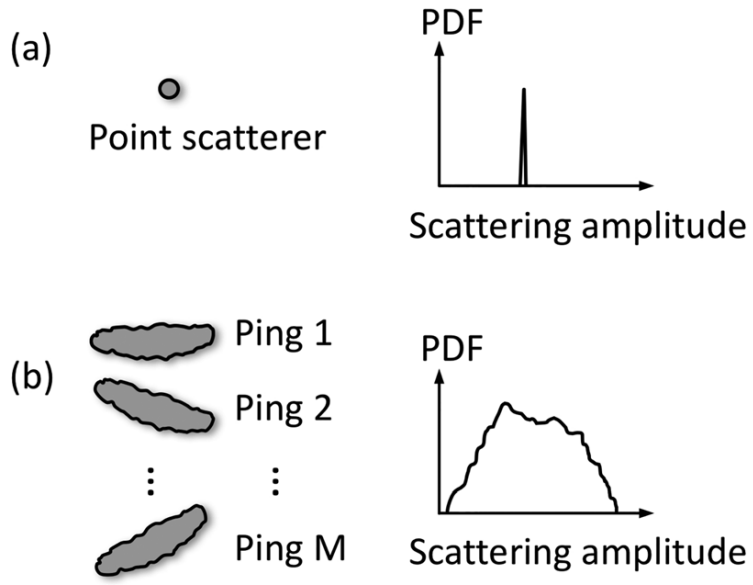

Figure 8. Echo Statistics of a Simple Target. Source: Stanton et al. (2018).

As more complexity is added (beampattern effects, multipath effects, additional scatterers, boundaries, discontinuities, etc.) the probability distribution will continue to change. If we consider our experimental scenario (turbulent plume), there are no discrete scatterers present. Any scattering is due to variations in temperature (and therefore sound speed), in particular, that from turbulent mixing. The expectation is that most echo returns will be indistinguishable and incoherent, resulting in continuous reverberation. It is often

reasonable to assume that continuous reverberation can be modelled by the Rayleigh probability distribution, this is due to the continuous nature of the scattering validating central limit theorem. When central limit theorem holds, the two fluctuating components (in-phase and quadrature) of the received complex acoustic backscatter signal tend towards Gaussian distributions with zero mean. The statistical distribution of the magnitude of the sum of these two components forms the Rayleigh PDF (Stanton et al. 2018). Any deviations from the Rayleigh distribution are of particular interest and may indicate the presence of discrete scatterers or an otherwise coherent signal within the noise.

When looking at the percentage of occurrence of a particular bin or range of backscatter amplitudes being met, the probability density function (PDF) is of most use. However, it is also useful to determine the sum, or integral of the PDF, known as the cumulative density function (CDF), and by extension the probability of false alarm (PFA). The PFA is given by 1-CDF and describes the probability that the amplitude will be higher than or equal to a given value. It is often used on a logarithmic scale to best illustrate the behavior of the high amplitude values at the tail of the distribution.

D. STATISTICAL DISTRIBUTIONS

The probability functions that are considered in this study are the: Rayleigh, Weibull, K, Rician, and log-normal distributions. These distributions are the most commonly used with respect to acoustic backscattering modelling, with each having been overserved from previous boundary and volume scattering studies. With the exception of the Lognormal distribution, all distributions have some analytical relationship to physical backscattering mechanisms (Gallaudet and Moustier 2003).

1. Rayleigh

The Rayleigh distribution is widely used for describing acoustic statistics (Stanton et al. 2018). High frequency backscatter from the surface and seafloor boundaries, and within the volume, have been observed to display Rayleigh characteristics (Gallaudet and Moustier 2003). The Rayleigh distribution relies on assumptions that are rooted in Central Limit Theorem, that is, that the real and imaginary parts of the received echo amplitude are

independent and normally distributed (Jakeman 1980). The statistical distribution of the magnitude of these real and imaginary components can be shown to be the Rayleigh PDF

$$f_R(x) = \left(\frac{2x}{\lambda}\right) e^{\frac{-x^2}{\lambda}} \tag{9}$$

where the associated CDF is

$$F_R(x) = 1 - e^{\frac{-x^2}{\lambda}} \tag{10}$$

As the Rayleigh distribution relies on the application of central limit theorem, it is of greatest usefulness when the number of scatterers is large (as is the case with continuous scattering), or there are many returns from an individual scatterer (Stanton et al. 2018). However, often in typical shallow water environments—due to the size, number and spatial distribution of the scatterers—these assumptions will not hold (Gallaudet and Moustier 2003), resulting in non-Rayleigh statistics. In these cases, the echo returns of the higher values (in the 'tail' of the distribution) are of most interest, as they have the greatest potential to cause clutter and interfere with the detection process (Stanton et al. 2015).

2. Weibull

The Weibull distribution is related to the exponential distribution and the Rayleigh distribution, and as such, it maintains a relationship to physical scattering mechanisms. It has been used to describe seafloor backscatter amplitude distributions (Lyons and Abraham 1999). The PDF for the Weibull distribution is

$$f_W(x) = \alpha\beta x^{\beta-1} e^{-\alpha x^{\beta}} \tag{11}$$

with the CDF

$$F_W(x) = 1 - e^{-\alpha x^{\beta}} \tag{12}$$

Special cases of the Weibull distribution occur when $\beta = 1$ or, $\beta = 2$ and $\alpha = 1/\lambda_{Ray}$, resulting in the Weibull distribution collapsing into the exponential distribution or the Rayleigh distribution respectively.

3. K

Like the Weibull, the K distribution maintains a connection to physical scattering mechanisms through a Rayleigh component. The distribution is a limiting case of the Rayleigh distribution, where instead of the sample size being without limit and central limit theorem holding, the sample size itself is a statistical variable (Jakeman 1980). This distribution has been shown to represent sonar reverberation from the seafloor (Abraham and Lyons 2002; Lyons and Abraham 1999), and has become a standard model for radar clutter (Ward 1981). It can be derived as the product of a Rayleigh distributed random variable and a chi distributed random variable, or a Rayleigh distribution whose mean square value is gamma distributed (Stanton et al. 2018). The PDF for the K distribution is

$$f_K(x) = \frac{4}{\sqrt{\alpha}\Gamma(\nu)}\left(\frac{x}{\sqrt{\alpha}}\right)^{\nu} K_{\nu-1}\left(\frac{2x}{\sqrt{\alpha}}\right) \tag{13}$$

and the CDF is

$$F_K(x) = 1 - \frac{1}{\Gamma(\nu)2^{\nu-1}}\left(\frac{2x}{\sqrt{\alpha}}\right)^{\nu} K_{\nu}\left(\frac{2x}{\sqrt{\alpha}}\right) \tag{14}$$

for $x \geq 0$, where K is the modified Bessel function, and Γ is the gamma function.

4. Rician

The Rician (or Rice) distribution was originally developed to describe a fixed signal in the presence of Gaussian noise (Stanton et al. 2018). It is often used in communications to model a fading signal with a stronger line-of-sight, as well as being used for noise analysis in magnetic resonance imaging (Koay and Basser 2006). For acoustic purposes the distribution has been applied to deep seafloor scattering (de Moustier 1986), and used to model fluctuating backscatter from fish (Stanton and Clay 1986). The PDF of the Rician distribution is

$$f_R(x) = \frac{x}{\sigma^2} e^{\frac{-\left(x^2+\nu^2\right)}{2\sigma^2}} I_0\left(\frac{x\nu}{\sigma^2}\right) \tag{15}$$

where I_0 is the zeroth order modified Bessel function of the first kind. The Rician CDF is

$$F_R(x) = 1 - Q_1\left(\frac{\nu}{\sigma}, \frac{x}{\sigma}\right) \tag{16}$$

where Q_1 is the Marcum-Q function. The Rician distribution is often re-written in terms of the power signal-to-noise ratio S, where

$$S = \frac{\nu^2}{2\sigma^2} \tag{17}$$

As S tends to zero the Rician distribution collapses into a Rayleigh distribution, and as S becomes large, the Rician distribution becomes Gaussian-like.

5. Log-normal

The log-normal distribution comes out of the weak scattering theory of Rytov and Born (Colosi 2016) and is more typically associated with forward scattering mechanisms. Despite this, observations of the log-normal distribution have been made in several studies of underwater acoustic backscatter, in particular that of bottom backscatter (Chotiros et al. 1986, Stanic and Kennedy 1992). The log-normal PDF is

$$f_{LN}(x) = \frac{1}{x\sqrt{2\pi\sigma^2}} e^{\frac{-(\ln x - \mu)^2}{2\sigma^2}} \tag{18}$$

with the CDF

$$F_{LN}(x) = \Phi\left(\frac{\ln x - \mu}{\sigma}\right) \tag{19}$$

where Φ is the CDF of a normally distributed random variable with unit variance.

THIS PAGE INTENTIONALLY LEFT BLANK

III. METHODOLOGY

A. INSTRUMENTATION

A suite of instruments was used in order to obtain all relevant data for the conduct of this experiment. The primary instruments with which we obtained the experimental data were the BioSonics DT-X range of echosounders. In addition to this, temperature and velocity sensors in the form of the RBR Duet and the Signature 1000 ADCP were also employed to characterize the experimental environment.

1. Biosonics DT-X Digital Scientific Echosounder

The principal instrument used in this experiment was the BioSonics DT-X digital scientific echosounder. The echo sounder is advertised as a *"compact, versatile echosounder that can be configured for many different applications in both marine and freshwater applications, including bathymetry, biology, habitat assessment and monitoring, population dynamics, behavior, and plant sediment distributions"* (Biosonics 2014). The DT-X kit consists of two parts, the first is the surface unit which is housed in a ruggedized case and contains the power supply, echosounder transmitter, associated cabling, and, the control computer. The second part is the echo sounder transducers (Figure 9).

Figure 9. Biosonics DT-X Echosounder. Source: Biosonics (2014).

The Biosonics sensors are high frequency and narrow bandwidth. The transducers are capable of operating in split beam or single beam mode, however for the experiment only single beam data was analyzed. Three Biosonics DT-X transducers were used for the experiment: 70kHz, 120kHz and, 200kHz. A proprietary software package called Visual Acquisition is also provided which allows the user to control and configure the echosounder, as well as utilize data logging, data playback and preliminary analysis features. For the conduct of the experiment Visual Acquisition was only used for configuration, control and quality control purposes. All data analysis was conducted via custom MATLAB code.

2. RBR Duet T.D.

The RBR Duet T.D. is a dual channel, compact, submersible temperature and depth sensor and data logger (Figure 10). This sensor is battery powered and is capable of sampling temperature and depth data at a rate of 2Hz to an accuracy of ±0.002°C and

±0.05% of depth scale respectively (RBR 2017). Sensor control and configuration is accessed by connecting the sensor to a PC via USB and using RBR's proprietary Ruskin software. Once data collection is complete the Ruskin software can again be used to access the data for basic analysis or to convert the data to a different format for processing via alternate software. For this experiment all data analysis was conducted via custom MATLAB code.

Figure 10. RBR Duet T.D. Temperature and Depth Sensor

3. Signature 1000 Acoustic Doppler Current Profiler

The Signature 1000 Acoustic Doppler Current Profiler (ADCP) is a five-beam current profiler designed for use in turbulent environments (Nortek 2018). The sensor operates at a center frequency of 1000 kHz with a maximum bandwidth of 25% (or 250 kHz) and has the ability to measure currents in 3 dimensions. Figure 11 shows the position of the transducers, where transducer five measures current in the vertical. Transducers one to four are angled from the horizontal, and in conjunction with transducer five, are used to triangulate current in the horizontal direction. The vertical transducer is also capable of providing echo sounder and high-resolution velocity data. This ADCP is able to sample at a maximum frequency of 16 Hz with a velocity resolution of 0.1 cm/s and an echo sounder

resolution down to 3 mm (Nortek 2019). The configuration and employment of the ADCP is controlled via Nortek's Signature Deployment software. On completion of the sensor deployment the data was able to be converted to MATLAB format with the Signature Deployment software. All data analysis was conducted via custom MATLAB code.

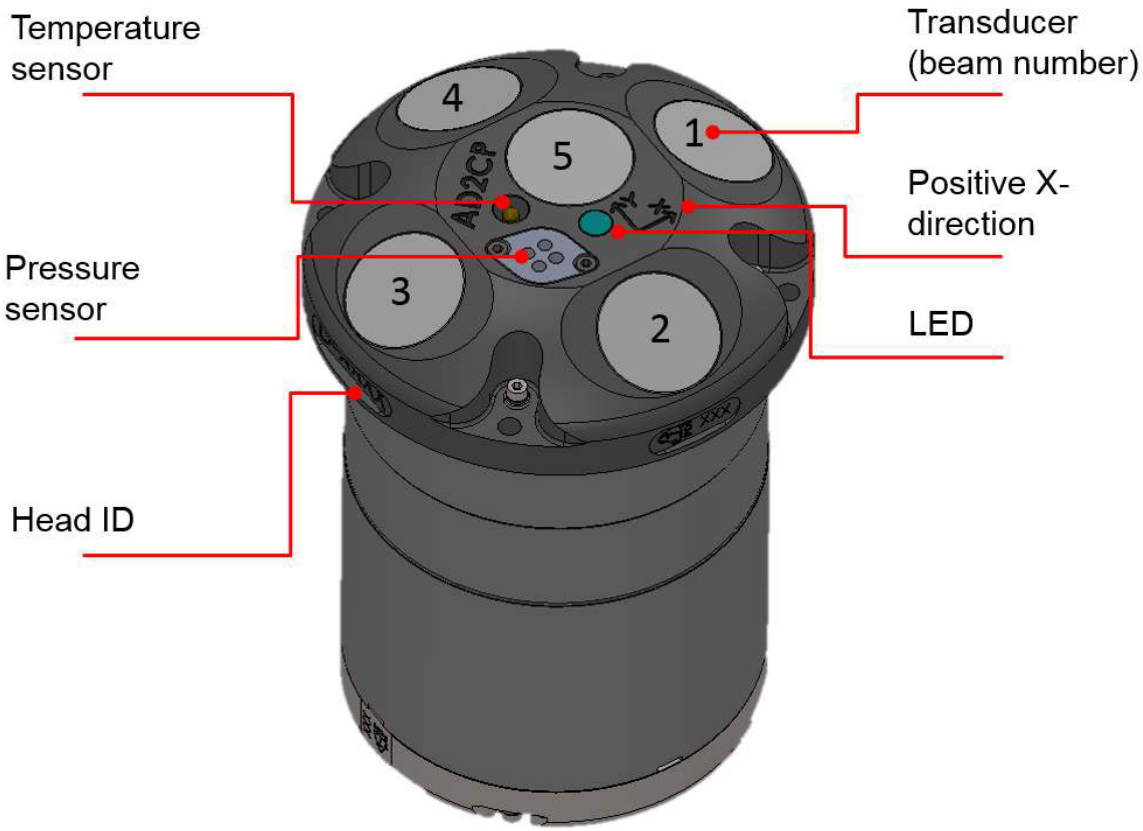

Figure 11. Signature 1000 ADCP. Source: Nortek (2018).

B. EXPERIMENTAL SETUP

The measurements of the high-frequency narrowband scattering through a turbulent plume were conducted on 11 and 12 March 2019, in the underwater acoustics teaching and research laboratory, located in the basement of Spanagel Hall, Naval Postgraduate School, Monterey.

The tank in which we performed the experiment measured 10 m length by 2 m width and 2 m depth, and was filled with fresh water. At one end of the tank we mounted a bucket comprising of a regular plastic pail of diameter 30 cm with a perforated false bottom (Figure 12). This bucket was filled with ice and mounted such that the bottom of the bucket sat approximately 3 cm below the waterline of the tank.

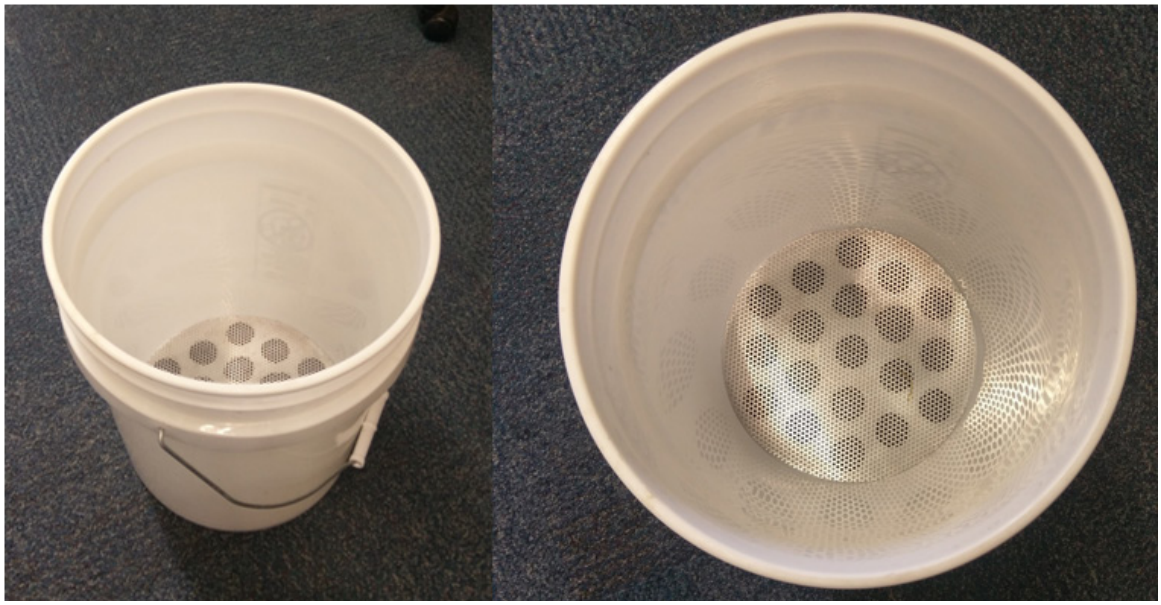

Figure 12. Ice Bucket Showing Perforated False-Bottom

At the other end of the tank were two Biosonics DT-X transducers, mounted such that they were horizontal facing, with one stacked on top of the other. The transducers were attached to steel brackets, which were then mounted to a rack made from round tubing which acted as the support base (Figure 13).

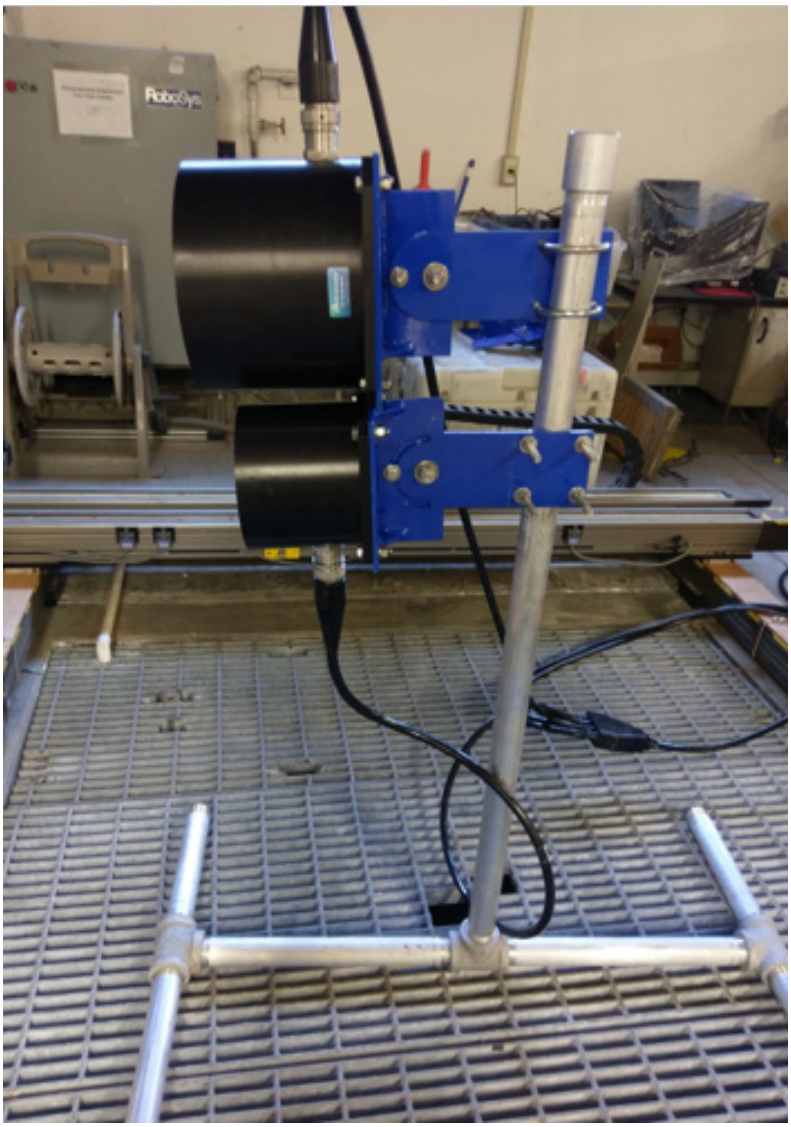

Figure 13. Mounting for DT-X Transducers

The rack was lowered into the tank such that the transducers were at the approximate half way depth (1 m) of the tank. The lateral displacement of the transducers from the ice bucket was determined by using the real-time data from the Visual Acquisition software to identify the position in which there was the least interference from side-lobes. This distance was approximately 3.1 m (Figure 14).

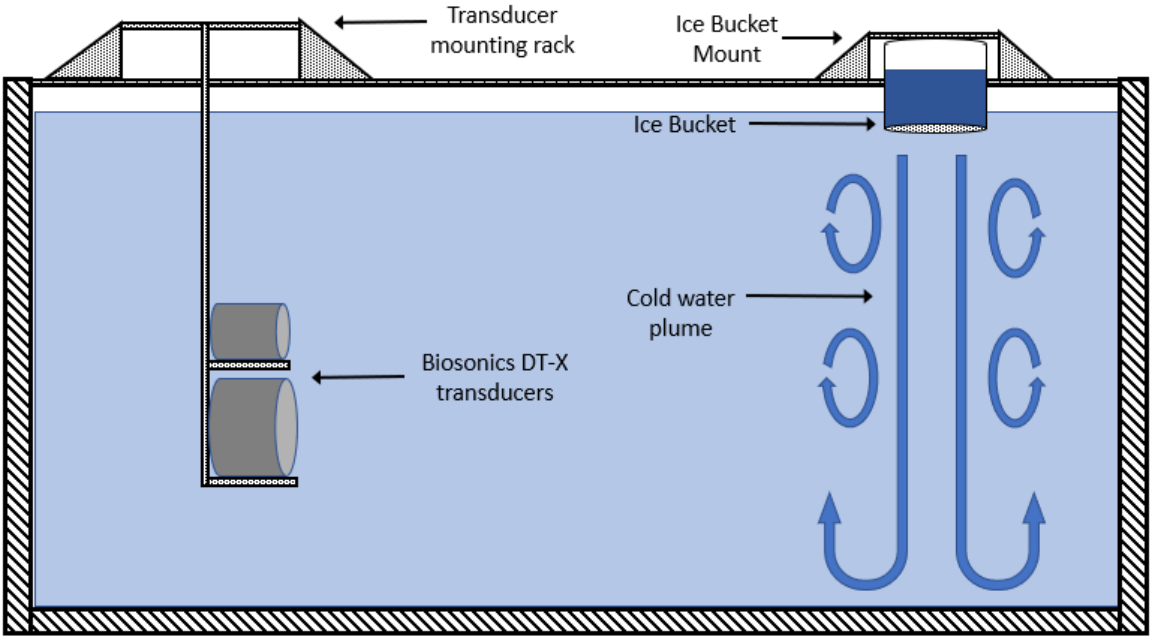

Figure 14. Experimental Tank Setup

The experiment was conducted over two days. On 11 March 2019, simultaneous data collection of 120kHz and 200kHz data was collected. On 12 March 2019 the experiment was repeated with simultaneous collection of 70kHz and 200kHz. During each experiment the transducers were placed in the water and commenced operating prior to the ice being added to the bucket. Once the experiment had begun the laboratory was vacated and locked. We returned approximately one hour later to cease the transducer operation and perform quality control and initial analysis on the data via the Visual Acquisition software. The settings used for the transducers throughout the experiment are listed in Table 1.

Table 1. Biosonics DT-X Settings

	11 Mar 2019	**12 Mar 2019**
Ping Rate	20Hz	20Hz
Pulse Duration	0.1ms	0.1ms
Range	0.1-10m	0.1-10m
Temperature	17.7°C	17.7°C
Speed of Sound	1474.3m/s	1474.3m/s

C. PHYSICAL PROPERTIES OF THE WATER COLUMN

To better understand the environment in which the experiment was conducted, we also set about conducting a series of experiments to characterize the physical properties of the water column. These characterization experiments were mutually incompatible with the primary echo sounder experiment, and as such could not be conducted simultaneously. From this secondary set of experiments, we extracted basic parameters which were useful in supporting the results from the echo sounder experiment.

1. Vertical Velocity Data

The first of the environmental characterization experiments was the use of the Signature 1000 ADCP to measure the vertical velocity at which the cold water within the turbulent plume sank. The ADCP was situated on the bottom of the tank, pointing upwards in the configuration shown below (Figure 15).

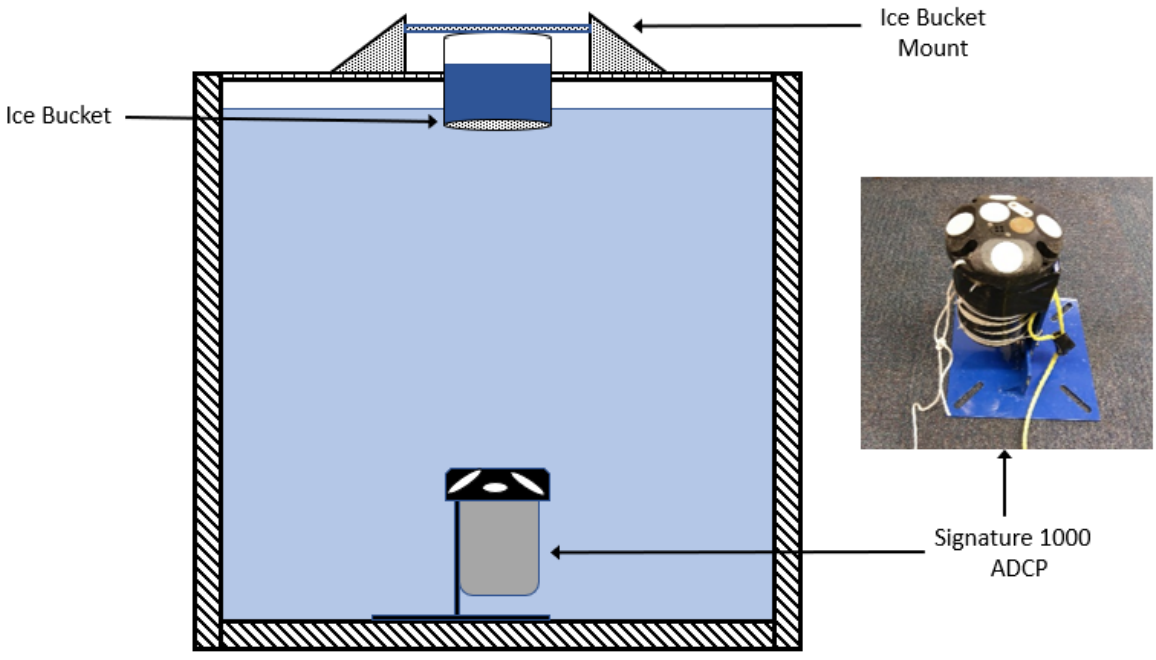

Figure 15. ACDP Experimental Setup

The ADCP was configured to collect both echo and velocity data from the water column with the following settings shown in Table 2.

Table 2. ADCP Settings

Echo Sounder Mode	**Current Profiler (High Resolution Mode)**
Frequency: 1000kHz	Frequency: 1000kHz
Sample rate: 4Hz	Sample rate: 4Hz
Range: 0.1 – 3m	Range: 0.1 – 3m
Cell size: 0.01m	Cell size: 0.02m
Transmit length: 0.05ms	Pulse distance: 3.35m

a. Echo Sounder Measurement

From the echo sounder and vertical velocity datasets we were able to visually identify vertical motion and measure the velocity of the plume respectively. Firstly, by looking at the echo sounder data, we were clearly able to identify that vertical motion was occurring, confirming that the cold-water plume was actively sinking. Figure 16 shows the echo sounder data from 500 seconds to 2000 seconds, the bright yellow streaks with a downward slope indicate the sinking water. During this time, we can also observe what appear to be spikes in activity at 600 and 800 seconds.

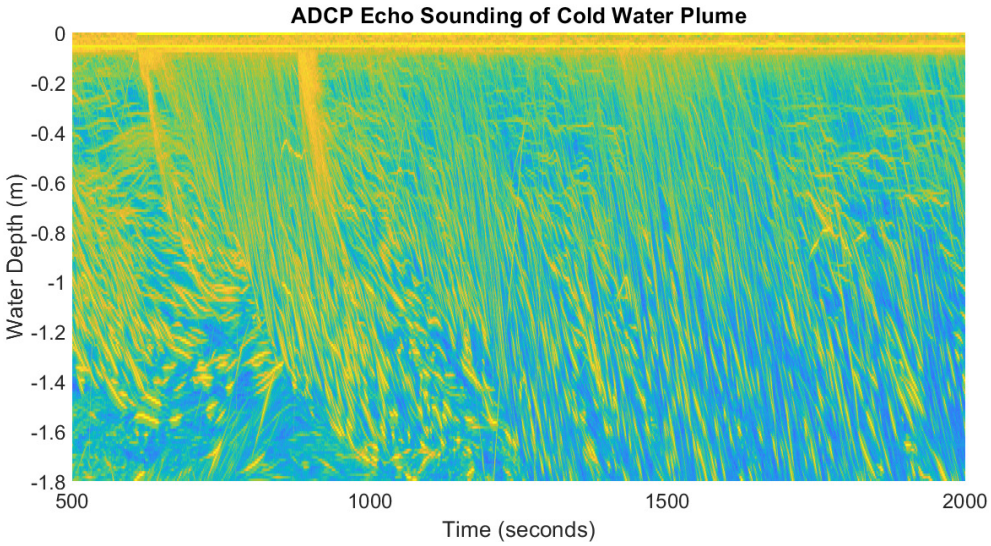

Figure 16. ADCP Echo Sounder Data Showing Vertical Motion of Cold Water

This echo sounder data was quite convincing and could also be used to approximate the vertical velocity of the plume. In Figure 17, the echo sounder data has been focused on the time period between 1500 seconds and 1700 seconds. The dashed black line shows a plume which can be traced from the surface of the tank to the bottom. The plume appears to be accelerating initially before slowing as it approaches the bottom of the tank. The approximate change in time (Δt) is observed at 140 seconds and the vertical distance (Δz) is 1.8m. From this we can approximate the average vertical velocity of the plume using the equation

$$w = \frac{dz}{dt} \approx \frac{\Delta z}{\Delta t} \tag{20}$$

This yields an average vertical velocity of 0.013 m/s.

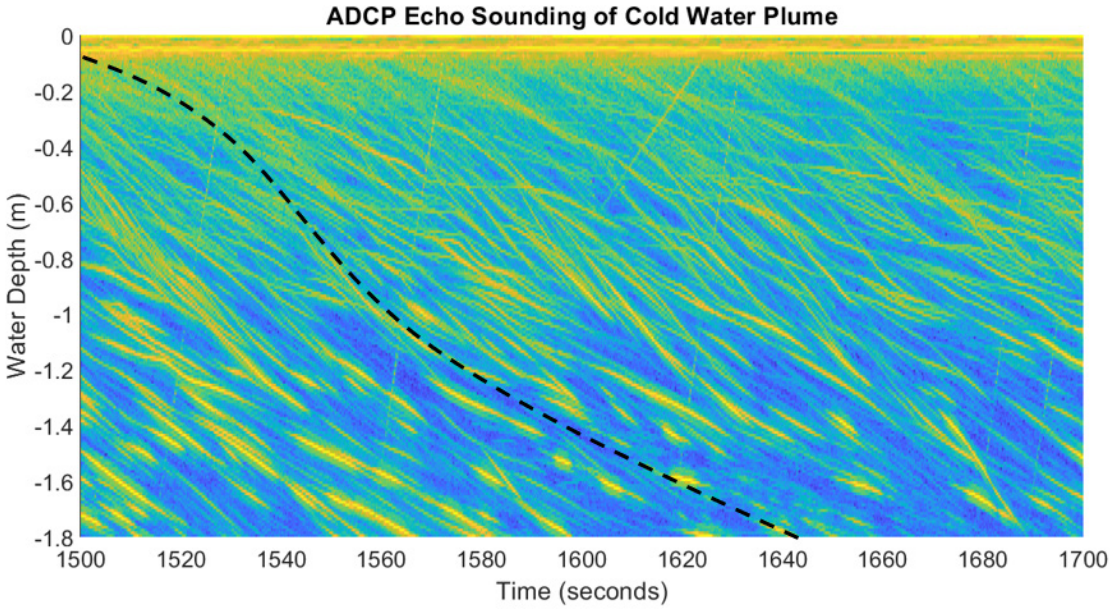

Figure 17. Zoomed in Echo Sounder Data Used for Vertical Velocity Calculation

b. Doppler Velocity Measurement

By looking at the high-resolution current data we were able to see a more detailed breakdown of the vertical velocity within the water column. In the figure below the mean vertical velocity has been calculated over the same 1500–1700 second window as used previously (Figure 18).

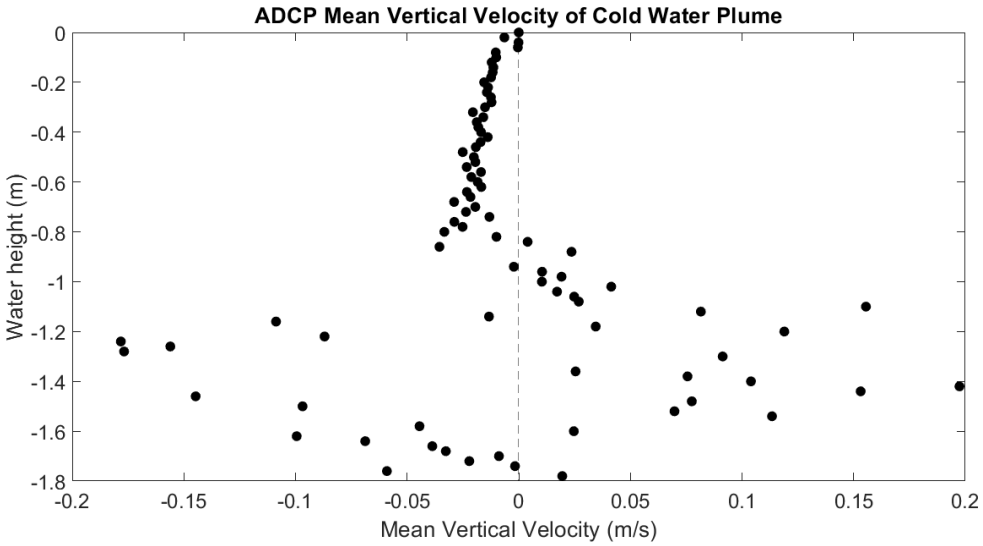

Figure 18. High Resolution ADCP Vertical Velocity Data

We are now able to identify the plume as a feature that appears as an accelerating free jet followed by a transition into a boundary layer as the jet impinges on the bottom of the tank. The average speed of the plume through the depth of the tank is observed to accelerate to 0.033 m/s at the 0.8 meter depth mark before becoming erratic. Overall, the mean vertical velocity through the entire depth of the tank is calculated to be 0.011 m/s, this compares well with the approximated echo sounder mean of 0.013 m/s. The average velocity of the entire plume prior to transition into a boundary layer (estimated at the 0.8 meter depth mark) is 0.0169m/s.

The high resolution ADCP data has given us instantaneous vertical velocity measurements, from which we have calculated the mean velocity. Now, from these two values we can use Reynolds decomposition (Equation 6) to determine the turbulent fluctuations and plot them against depth (Figure 19).

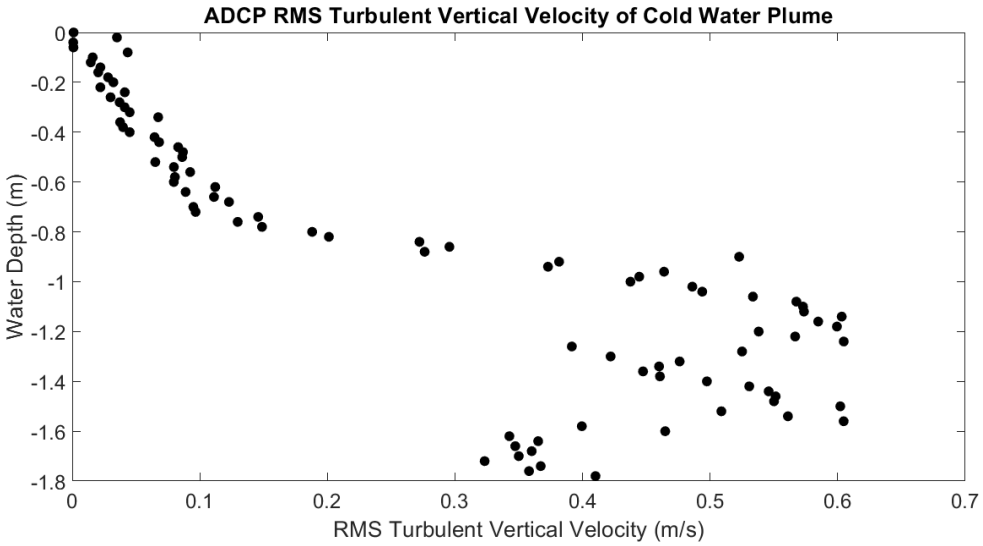

Figure 19. RMS Turbulent Vertical Velocity

Here, we see a steady increase in turbulent velocity up to the 0.8 meter depth where the flow appears to become fully turbulent. This agrees well with our model of an accelerating free jet transitioning into a boundary layer as it impinges on the bottom of the tank. Also of importance from this result is that we can use the turbulent vertical velocity alongside the mean vertical velocity to approximate the applicability of Taylor's hypothesis. Looking only at the region prior to the transition to the boundary layer (0-0.8 m), we previously calculated an average velocity ($\bar{\mathbf{u}}$) of 0.0169 m/s. Within that same region the average turbulent fluctuation ($\mathbf{u}_{rms}$) is 0.0614 m/s. Thus, the ratio of these values is 3.6, which is not $\ll 1$, therefore the application of Taylors hypothesis will be of questionable accuracy for this experiment.

c. Reynolds number

With the vertical velocity value observed via the ADCP we can now approximate a Reynold's number based off the characteristic scales the plume. First, we assume that the characteristic length scale of the flow is given by the bucket diameter, that is L=0.3 m. Next, let the characteristic velocity scale be the calculated mean velocity of the entire column prior to impingement, that is U=0.0169 m/s. The viscosity (v) value is taken from

table A.3 in Kundu et al. (2012), and interpolated linearly for the mean water temperature of 17.3°C, resulting in $\nu = 1.225 \times 10^{-6}$ m^2/s.

So, via Equation 5, we find that Re = 4139. If our experiment was concerned with flow in a pipe then this Reynolds number would infer that the flow is turbulent, and although this is not the case since we are working with a plume, we can still use this result to reasonably assume that we have a turbulent flow.

d. Velocity Spectral Analysis

Spectral analysis of the velocity time series data was conducted to further probe the nature of the turbulent fluctuations within the plume. The timeseries as recorded at the one meter depth mark was chosen at it would be most representative of the backscatter area for the echo sounder experiment. The same 25 minute window of data as seen in Figure 16 was used, and the time series was split into 5 minute Hanning windows with 50% overlap. The normalized frequency spectrum at the 1 m depth is shown in Figure 20.

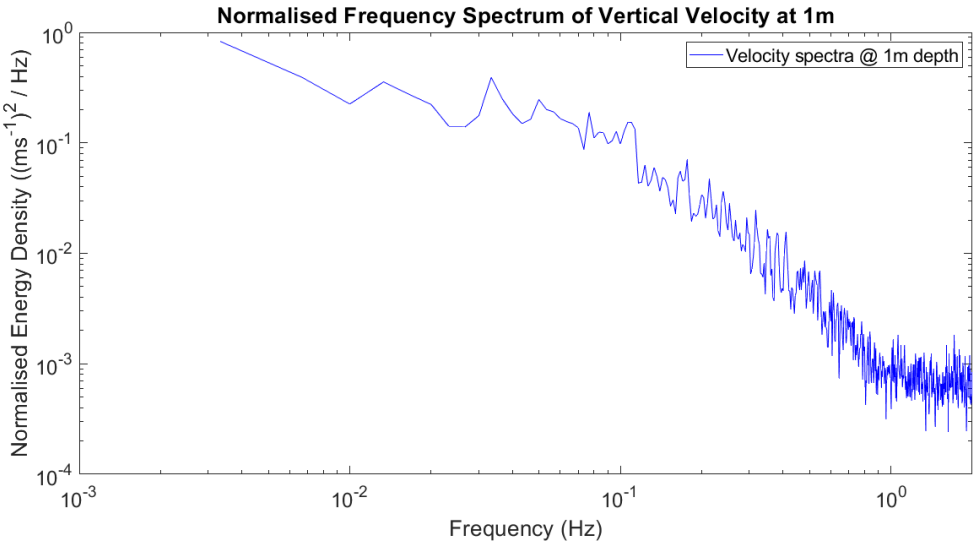

Figure 20. Vertical Velocity Frequency Spectrum at 1m Depth

This velocity frequency spectrum is not particularly useful in this context, so, assuming that Taylor's hypothesis holds, the frequency spectrum was transformed into a

wavenumber spectrum by using the mean velocity of 0.033 m/s at the probe location. The resulting plot is shown in Figure 24.

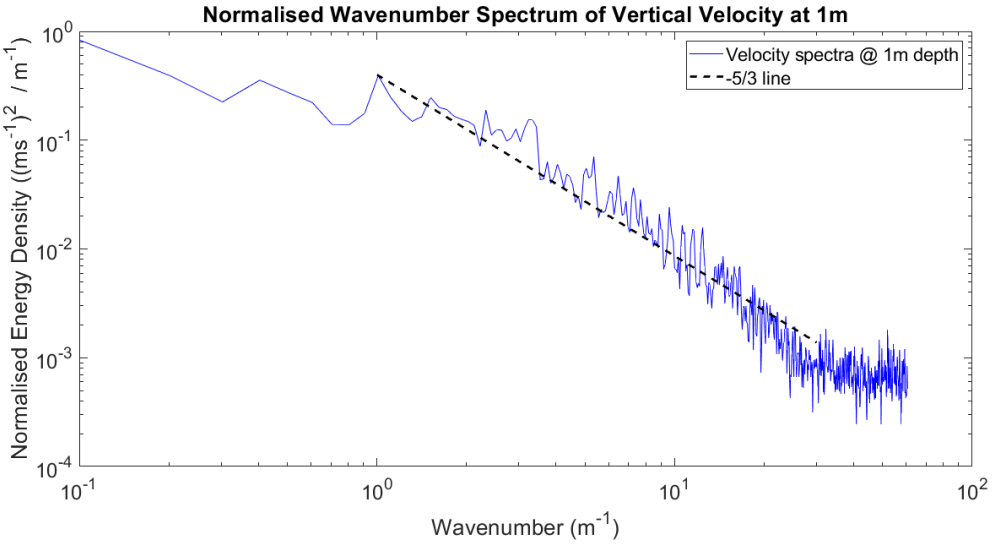

Figure 21. Vertical Velocity Wavenumber Spectrum at 1m Depth

The velocity wavenumber spectrum displays the classic -5/3^{rds} energy decay associated with Kolmogorov's theory and thus identifies the inertial subrange through which the energy cascade is occurring. This confirms that there is turbulent motion within the plume. The energy cascade tapers off and appears to approach a noise floor into the higher wavenumbers as we approach the Nyquist frequency. Due to the maximum sampling rate limitations of the sensor (4 Hz) and the presence of the noise floor we are unable to identify the Kolmogorov scale and therefore the scale at which viscous dissipation begins to play a role.

2. Temperature Data

The second of the environmental characterization experiments was the use of the RBR Duet temperature sensors to measure the environmental temperature changes due to the presence of the cold water plume. The temperature sensors were constructed in an array with a vertical separation of 80 cm between each sensor. The arrays were deployed directly

underneath the bucket (with the first sensor recording data at a depth of 20 cm) as well as 20cm offset from the bucket. The configuration is shown in Figure 22.

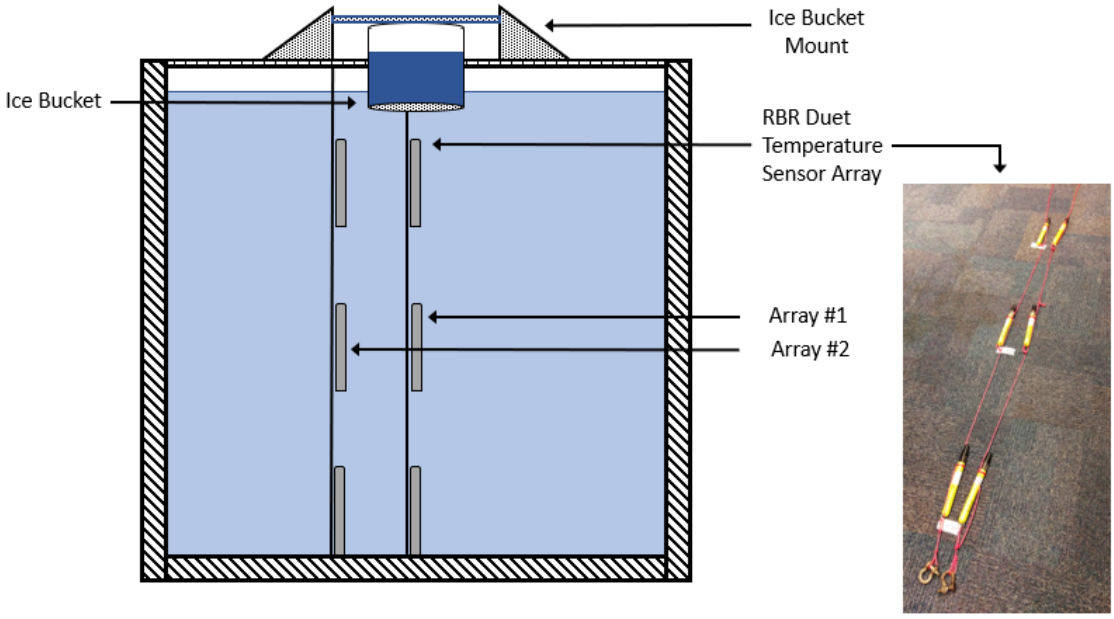

Figure 22. Temperature Array Experiment Setup

From these sensors we were able to construct temperature time series for all probes. This enabled us to conduct a basic analysis of the thermal plume including: extracting basic statisitics (mean, max and rms), estimate buoyant acceleration, velocity, and conduct a spectral analysis.

a. Temperature Time Series

By plotting the temperature data as a time series we can immediately get a feel for how the temperature fluctuates with time throughout the tank. Figure 23 illustrates this for six different locations within the tank over the course of an hour. Of note, is that the largest variations in temperature are seen directly below the bucket (blue line on leftmost plot), which slowly begin to decay from the 1500 second mark. This contrasts with the offset probe at the same depth (blue line, rightmost plot) where we see almost no temperature variations at all, suggesting that there is no lateral mixing at that depth. At the middle depth

(red line) we do see variations at both the directly beneath bucket and offset locations, suggesting that the plume has spread at least beyond the edge of the bucket at that depth. Both bottom location probes (green line) show next to no temperature fluctuations, suggesting that the plume is well mixed, this ties in well with our assumptions from the vertical velocity data that a boundary layer has formed at the bottom.

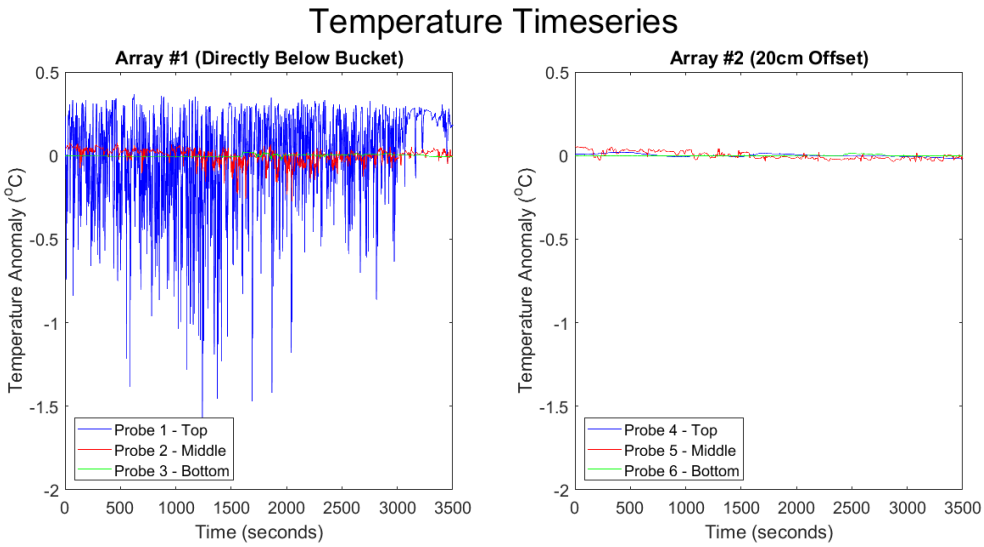

Figure 23. Temperature Timeseries

The basic statistics which we extracted from the time series were mean temperature, max and min temperature, and standard deviation. From the temperature statistics we also calculated the mean density and maximum density difference and mean speed of sound and maximum speed of sound difference. The statistics support what was observed in the time series as we only see significant variability ($\mathbf{T}_{\mathbf{rms}}$) in the sensor directly below the bucket (probe 1), followed by the two middle sensors (probes 2 and 5). All other probes show very weak temperature fluctuations. The density and sound speed data shows that the largest variations in density and sound speed are found directly beneath the bucket, with a slight drop in mean sound speed also occurring beneath the bucket.

Table 3. Temperature Timeseries Statistics

	Probe					
	1	**2**	**3**	**4**	**5**	**6**
$\mathbf{T_{mean}}$ **(°C)**	17.29	17.32	17.28	17.54	17.32	17.28
$\mathbf{T_{max}}$ **(°C)**	17.66	17.40	17.31	17.57	17.38	17.29
$\mathbf{T_{min}}$ **(°C)**	15.71	17.05	17.25	17.51	17.28	17.27
$\mathbf{T_{rms}}$ **(°C)**	0.28	0.04	0.01	0.01	0.02	0.00
$\boldsymbol{\rho_{mean}}$ **(kg/m^3)**	998.72	998.72	998.74	998.68	998.72	998.74
$\boldsymbol{\Delta\rho}$ **(kg/m^3)**	0.33	0.06	0.01	0.01	0.02	0.00
$\mathbf{c_{mean}}$ **(m/s)**	1473.76	1473.86	1473.73	1474.57	1473.86	1473.72
$\boldsymbol{\Delta c}$ **(m/s)**	6.56	1.15	0.17	0.17	0.31	0.06

If we average the data over each array, we see that there is only a 0.27m/s decrease in sound speed from the 20cm offset to the bucket center. This is an order of magnitude smaller than the maximum sound speed fluctuations averaged beneath the bucket of 2.62m/s.

b. Buoyancy Force

The time series statistics were also used to estimate the buoyant plume acceleration and velocity via reduced a gravity calculation (Equation 2). Table 3 provides the mean temperature and change in temperature at each depth. From that, we can then calculate the mean density and change in density (ρ_0 and $\Delta\rho$), and assuming g = 9.8m/s^2 we can calculate the reduced gravity at each depth. Plotting the reduced gravity vs depth and assuming an exponential decay allows us to integrate to find the velocity (in an Eulerian frame of reference). These two values are illustrated in Figure 24. Also shown in this figure for reference are the observed vertical velocities from the ADCP experiment (conducted independently), the ADCP values align well with the calculated velocity.

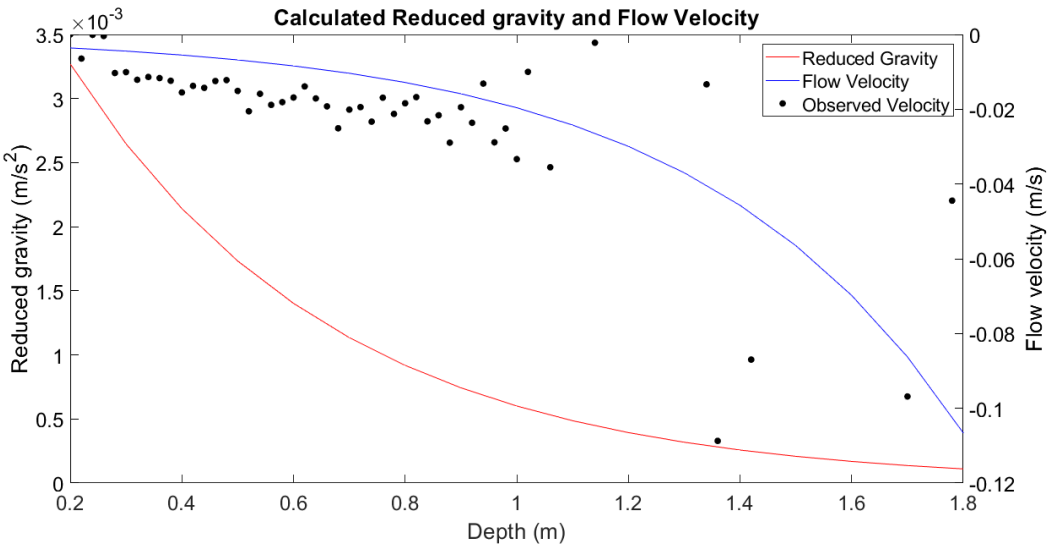

Figure 24. Reduced Gravity and Velocity of the Plume with Depth

c. Temperature Spectral Analysis

In the same manner as the velocity data, spectral analysis of the temperature time series data was conducted to further probe the nature of the turbulent fluctuations within the plume. The middle probe (depth 1 m) location directly beneath the bucket was chosen at it would be most representative of the backscatter area for the echo sounder experiment. The 60 minute time series was split into 30 minute Hanning windows with 50% overlap. The normalized frequency spectrum at the 1 m depth is shown in Figure 25.

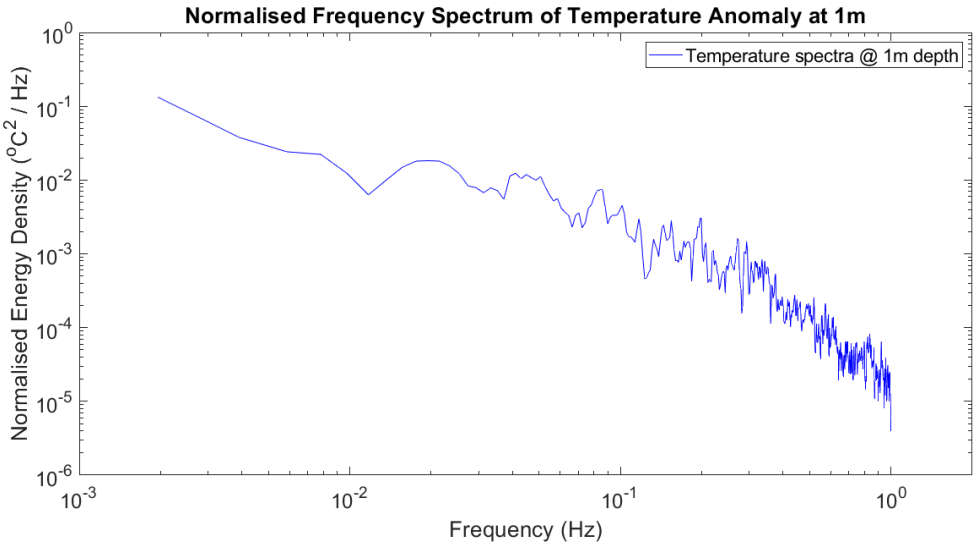

Figure 25. Temperature Frequency Spectrum at 1m Depth

Again, the frequency spectrum is not particularly useful in this context, so, maintaining the previous assumption that Taylor's hypothesis holds, the frequency spectrum was transformed into a wavenumber spectrum by using the mean velocity of 0.033 m/s at the probe location. The result is shown in Figure 26.

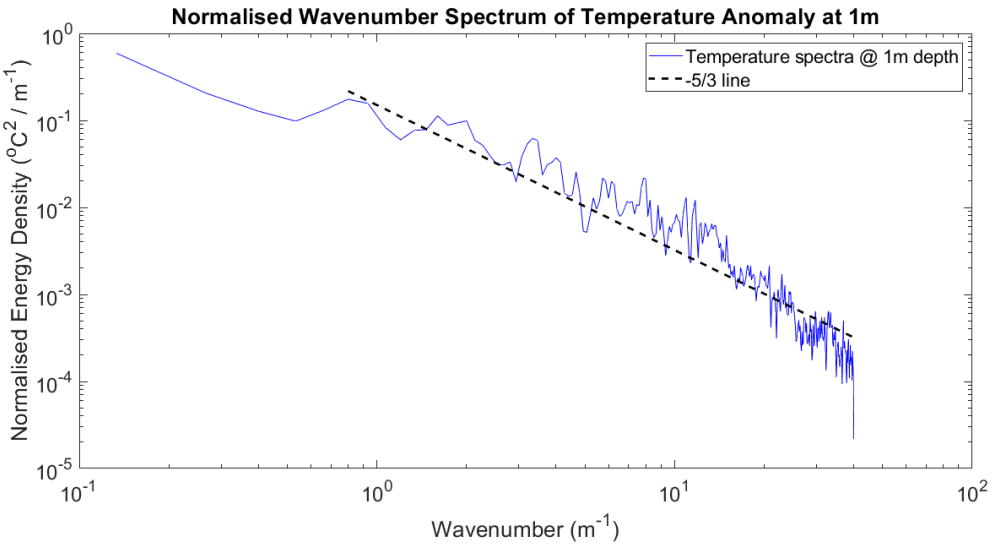

Figure 26. Temperature Wavenumber Spectrum at 1m Depth

Like the velocity spectrum, the temperature wavenumber spectrum displays the classic -5/3^{rds} energy decay associated with Kolmogorov's theory and thus identifies the inertial subrange through which the energy cascade is occurring, providing further evidence that there is turbulent motion within the plume. Again, due to the maximum sampling rate limitations of the sensor (2 Hz) we are unable to identify the Kolmogorov scale and therefor the scale at which viscous dissipation begins to play a role.

THIS PAGE INTENTIONALLY LEFT BLANK

IV. DATA ANALYSIS AND RESULTS

As seen in the temperature timeseries (Ch III.C.2.a) the turbulent fluctuations tended to decrease rapidly with time, indicating that the data is non-stationary. This decrease was also observed in the acoustic backscatter from the experimental echo sounder data. As such, the echo sounder timeseries would first need to be trimmed to maintain an acceptable signal to noise ratio for the statistical analysis, and then detrended. A 10dB cut off above the noise floor was chosen for the 120kHz and 200kHz data. The scattered power from the 70kHz transducer was much weaker, resulting in a significantly smaller signal-to-noise ratio, a 6dB cut off was used instead of 10dB so that an acceptable number of data samples could be obtained. In order to calculate the time interval over which the data was trimmed, the one second mean echo strength through the center of the turbulent plume was plotted against time. When plotted this way the plume center one second mean backscatter strength (in dB) showed a highly linear decay with time. A linear regression was conducted for all data sets, and when the mean backscatter strength line-of-best-fit dipped below the cutoff all further data was omitted. Figures 27 through 30 illustrate this process for all datasets.

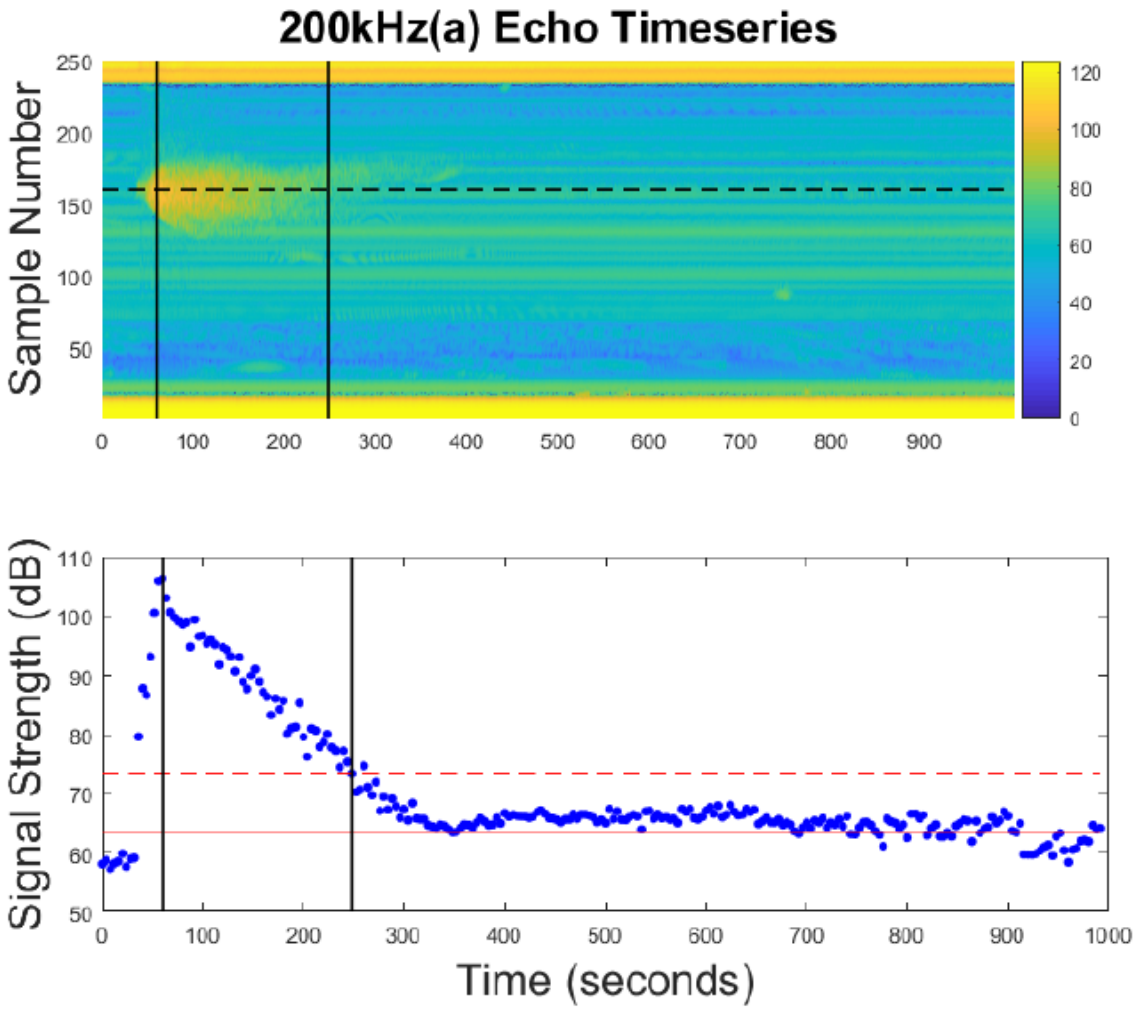

The top panel shows the 2-D timeseries of 200kHz data from 11 Mar 2019. Y-axis indicates distance from transducer (or sample number received by transducer) with X-axis as time, and color as echo strength. The yellow blob indicates the turbulent disturbance. The dashed black line indicates the plume center from where the one second mean was calculated. The bottom panel shows the backscatter strength timeseries through the plume center. Blue dots indicate the one second mean backscatter strength, the solid red line is the noise floor (calculated over the last half of the timeseries), and the dashed red line is the 10dB cut off above the noise floor. The trimmed dataset used for the analysis is indicated between the two black lines in both panels.

Figure 27. 200kHz(a) Echo Sounder Timeseries

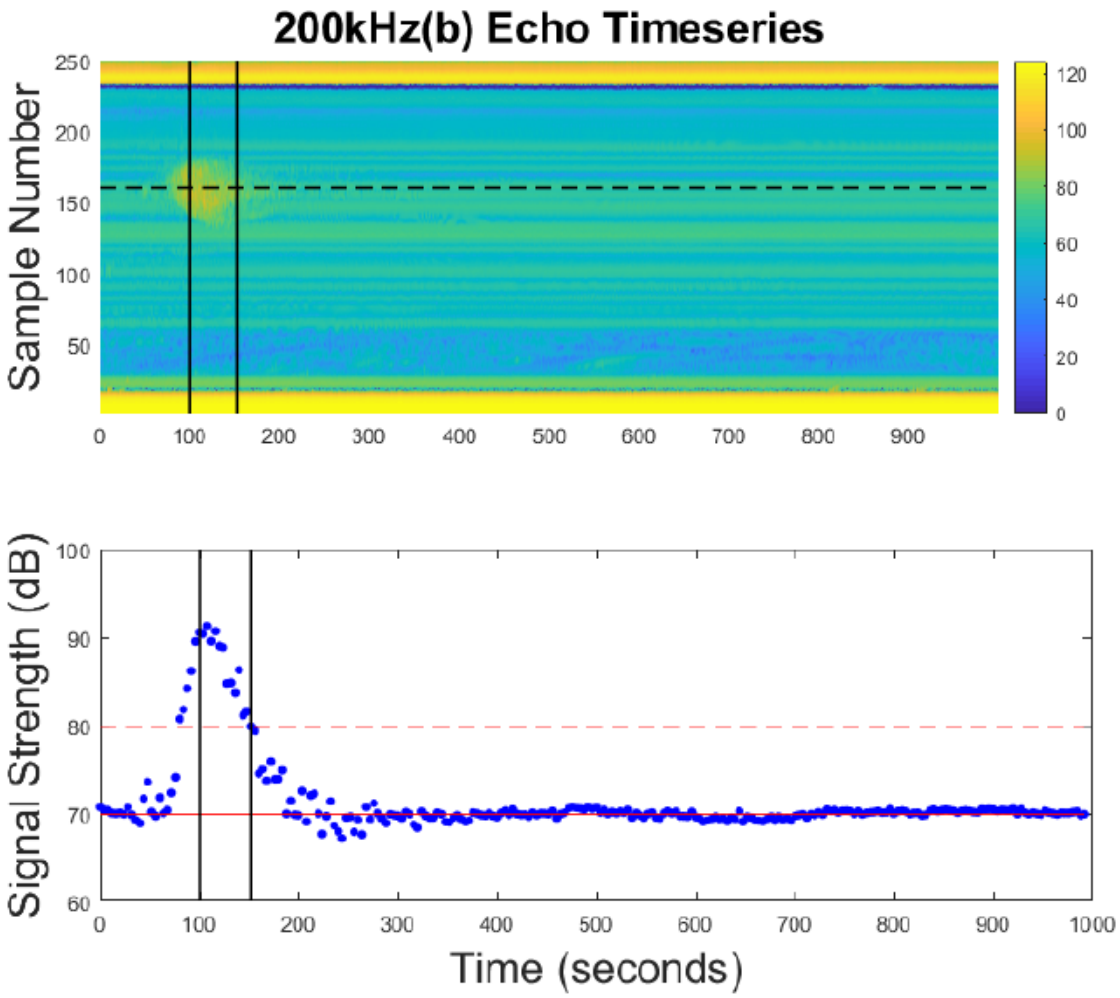

Timeseries of 200kHz data from 12 Mar 2019. Of note is that the signal strength is weaker than that observed in the 11 Mar 2019 experiment, leading to a smaller trimmed timeseries and less datapoints for the analysis. The trimmed dataset used for the analysis is indicated between the two black lines in both panels.

Figure 28. 200kHz(b) Echo Sounder Timeseries

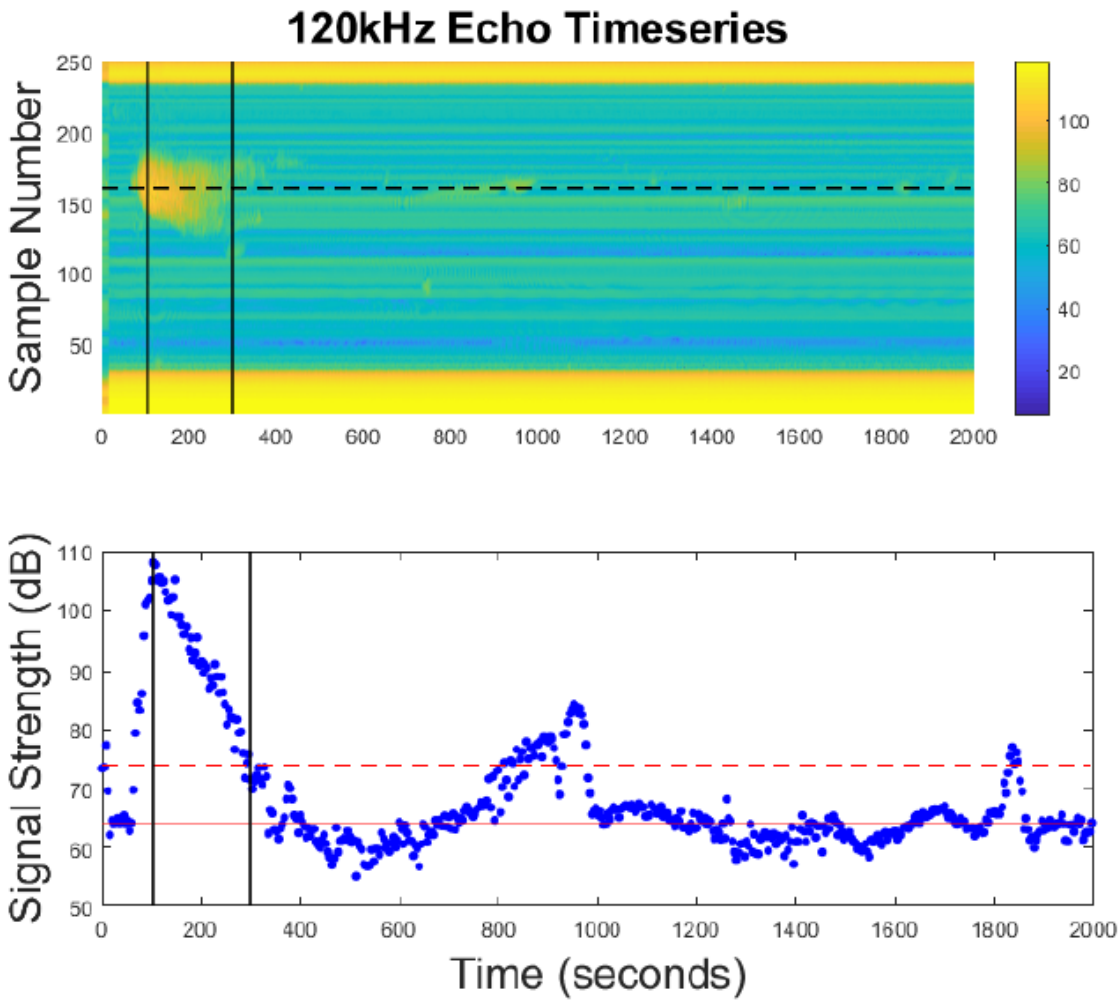

Timeseries of 120kHz data from 11 Mar 2019. After the initial turbulence event, we observe a secondary event at 800 seconds and a tertiary event at 1800 seconds, this is similar to the spikes in activity seen in Figure 16, however they were not considered for the analysis. The trimmed dataset used for the analysis is indicated between the two black lines in both panels.

Figure 29. 120kHz Echo Sounder Timeseries

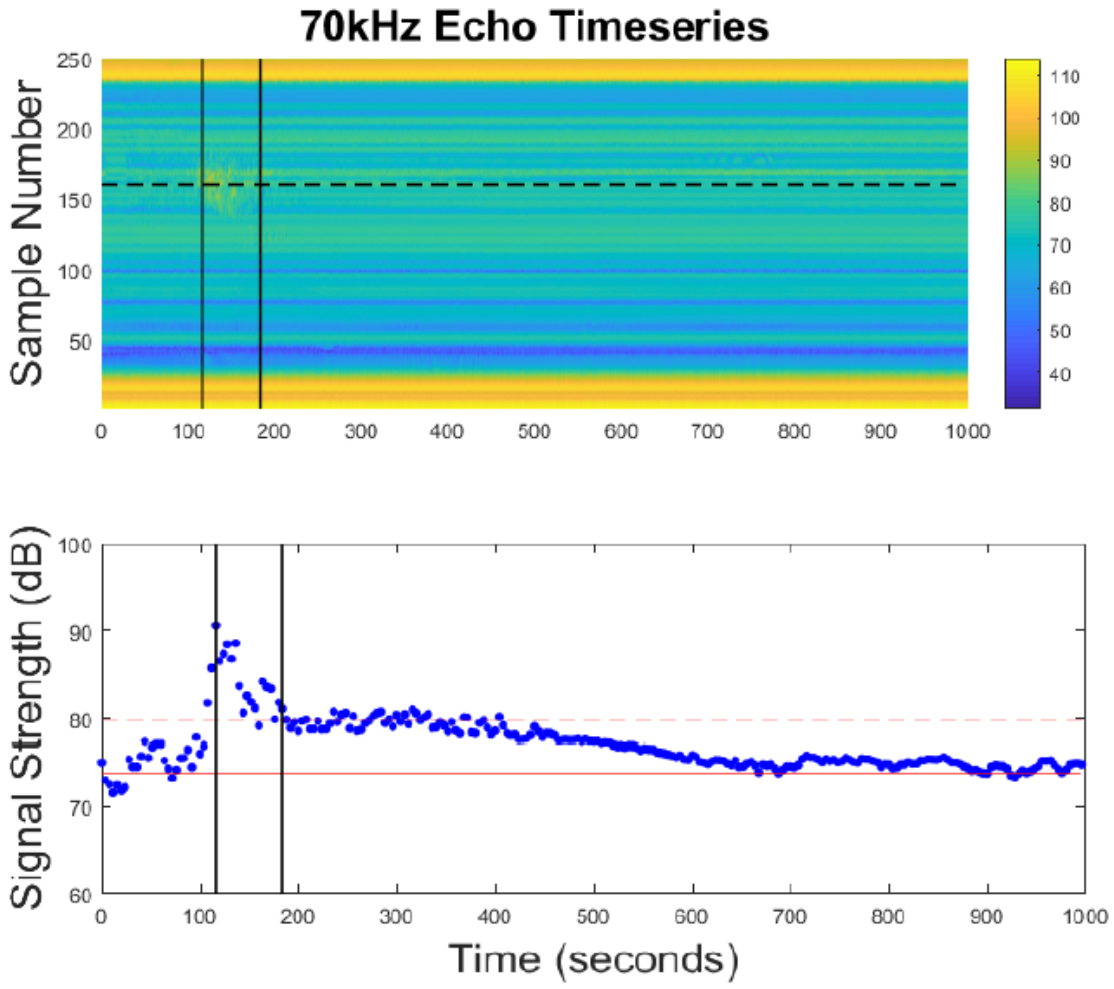

Timeseries of 70kHz data from 12 Mar 2019. This timeseries had the weakest backscattering strength of all. As a result, a 6dB cut off above the noise floor was used instead of 10dB so that an acceptable number of data samples could be obtained. The trimmed dataset used for the analysis is indicated between the two black lines in both panels.

Figure 30. 70kHz Echo Sounder Timeseries

After trimming the datasets, they were decimated in order to provide statistically independent data. Auto-correlation was conducted on each data set, with the decorrelation scale determined via the e-folding technique. The decimation factor was then based of the ping rate of 20Hz (Table 1). For example, the 70kHz data decorrelates in 0.25s whilst recording data at 20Hz, so five samples are recorded prior to decorrelation. If we wish to have statistically independent data, we can only use every fifth data point. Thus, the 70kHz

data has a decimation factor of five. Decorrelation time and data decimation factors are listed in Table 4.

Table 4. Decorrelation Time Scale and Decimation Factors

Sensor	Decorrelation time	Decimation factor
70kHz	0.25 seconds	5
120kHz	0.20 seconds	4
200kHz(a)	0.10 seconds	2
200kHz(b)	0.10 seconds	2

As we are only interested in the backscatter fluctuations, a cell averaging constant false alarm rate (CFAR) technique was used in order to detrend the large-scale power loss with time (Ghandi and Kassam 1988). The result of this process is a stationary timeseries of the reverberation fluctuations. The data was then partitioned into three zones, which represented the transition into the turbulent plume across the shear layer (which we have called the shear layer near, or SLN), through the fully-developed zone within the plume (called the plume center, or PC), and exiting from the turbulent plume (called the shear layer far, or SLF). Transects through each of these zones were then taken, with the data collected to represent each of the reverberation samples. An example of the transects representing the zones (black lines) through a trimmed, decimated and detrended dataset is shown in Figure 31. Finally, the data was normalized against the rms amplitude ($\langle A^2 \rangle^{\frac{1}{2}}$) value for each dataset as recommended by Stanton et al. (2018).

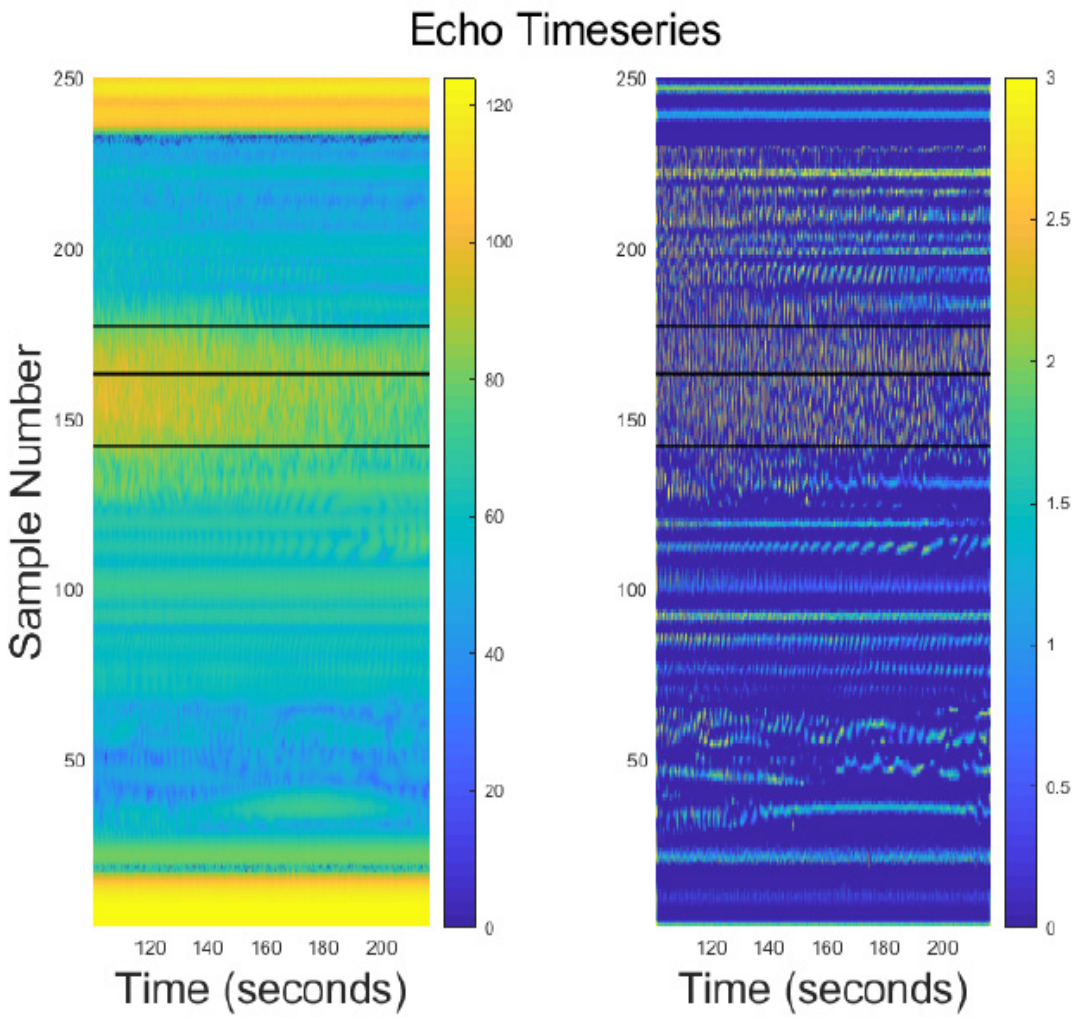

200kHz data from 11 Mar 2019. The left panel shows trimmed, non-detrended data. The right panel shows the trimmed, decimated and detrended data. Black lines indicate estimated position of SLN, PC and SLF (at sample numbers 142, 163, 177 respectively).

Figure 31. 200kHz(a) Turbulent Plume Zone Transects

A. SCATTERING STATISTICS

A statistical analysis was then conducted on each of the trimmed, decimated, detrended, partitioned and normalized datasets, allowing us to characterize the data by making statistical estimates of: mean normalized amplitude (μ_A), mean intensity (μ_{A^2}) variance (σ^2_A) and scintillation index (SI) (Table 5). The scintillation index (or the variance of the intensity) is of particular interest as a value of unity represents Rayleigh

distributed data (Flatté 1983; Colosi 2016). Any variation from this value provides an indication as to the non-Rayleigh nature of the data. As seen in Table 5 all scintillation index values are close to, but less than unity. This indicates that the data is close to being Rayleigh distributed, but that it may not be the best fit.

Table 5. Backscattering Statistics

Frequency	Zone	Sample Size N	Mean normalized amplitude μ_A	Mean intensity μ_{A^2}	Range	Variance σ^2_A	Scintillation index SI
70kHz	SLN	160	0.908	1.000	2.299	0.176	0.877
	PC	160	0.892	1.000	2.124	0.206	0.849
	SLF	160	0.941	1.000	1.523	0.115	0.406
120kHz	SLN	1060	0.911	1.000	2.310	0.170	0.740
	PC	1060	0.887	1.000	2.584	0.213	0.937
	SLF	1060	0.905	1.000	2.546	0.180	0.769
200kHz (a)	SLN	1160	0.901	1.000	2.679	0.188	0.856
	PC	1160	0.895	1.000	2.377	0.198	0.840
	SLF	1160	0.902	1.000	2.486	0.187	0.807
200kHz (b)	SLN	640	0.896	1.000	2.305	0.196	0.866
	PC	640	0.901	1.000	2.387	0.189	0.809
	SLF	640	0.913	1.000	2.024	0.167	0.612

B. PROBABILITY DISTRIBUTION FUNCTIONS

Parameters for the Rayleigh, Weibull, K, Rician and lognormal probability distribution functions were estimated from the echosounder amplitude data for each frequency and zone. These probability functions were then compared against the empirical probability distributions. Figures 32–34 show the results as probability of false alarm (PFA) vs the normalized amplitude, where, as mentioned in Ch II.C the PFA is the probability that the amplitude will be higher than or equal to a given value. The data are also presented on a logarithmic scale so to better demonstrate the departure of the empirical data from the PDF fit, which is most often found in the tail of the distribution.

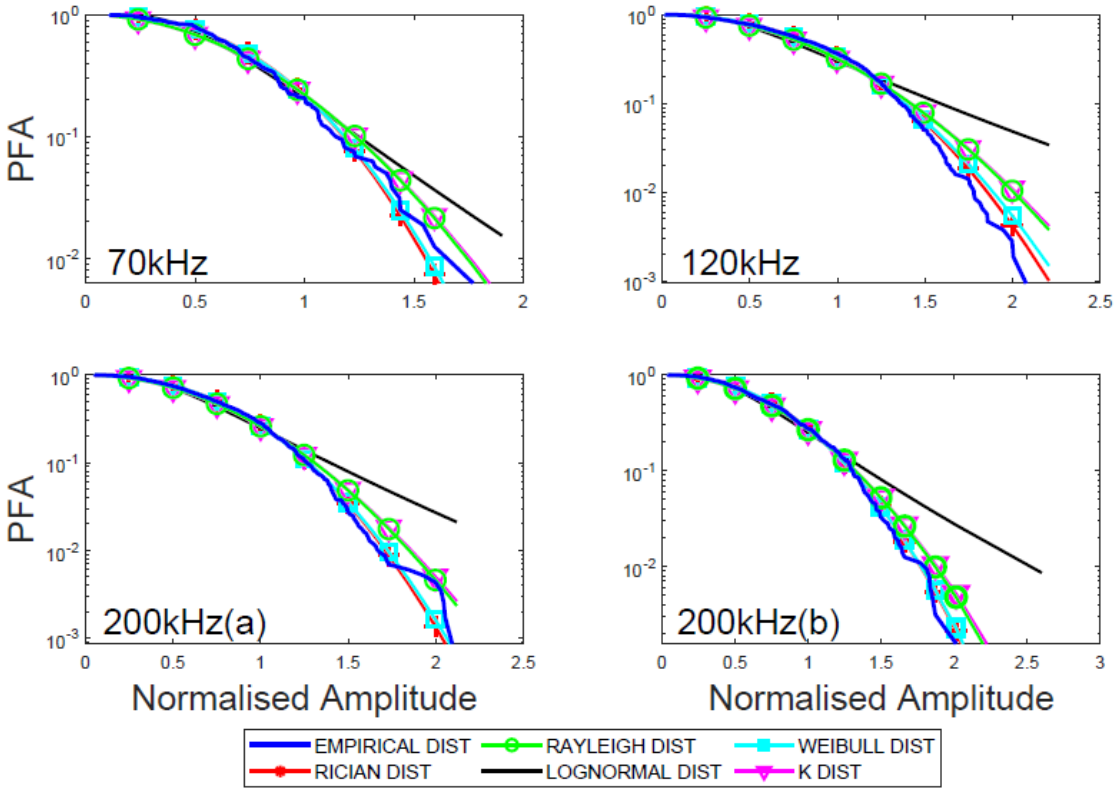

PFA vs Normalized Amplitude for the shear layer near zone. All subfigures indicate an empirical distribution within the sub-Rayleigh regime. 200kHz(a) refers to data collected during the 11 Mar 19 experiment, 200kHz(b) refers to data collected during the 12 Mar 19 experiment.

Figure 32. Probability of False Alarm: Shear Layer Near

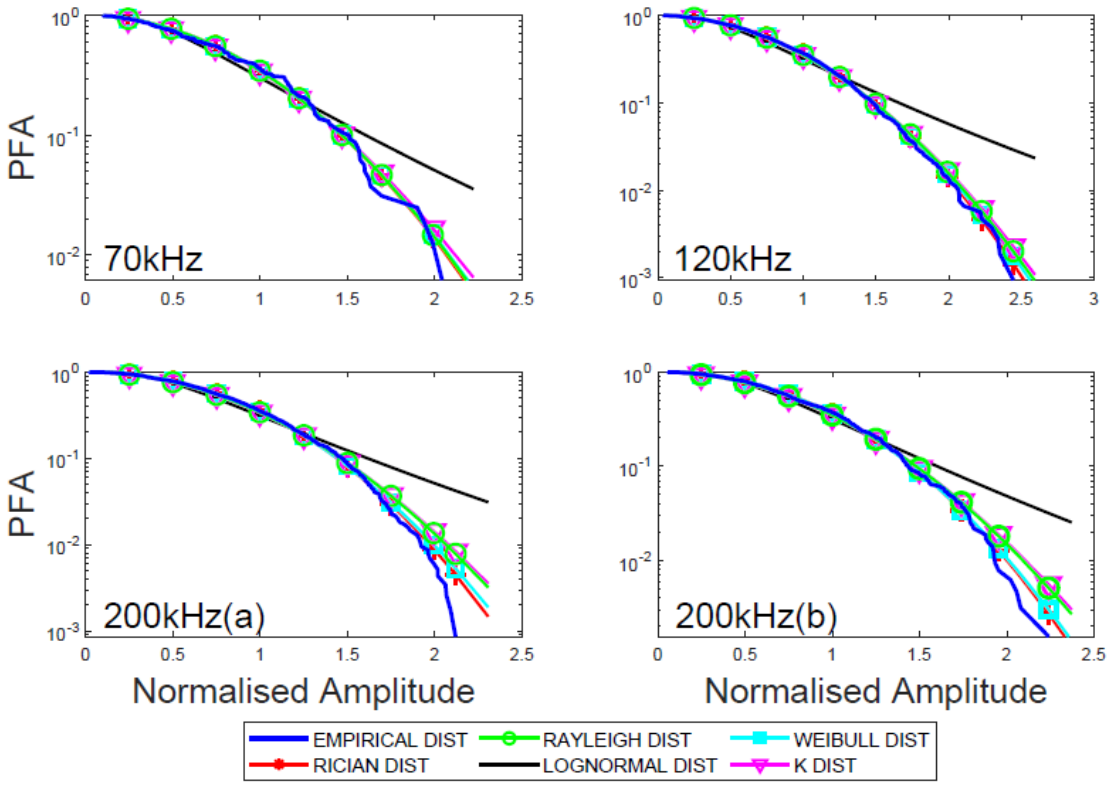

PFA vs Normalized Amplitude for the plume center zone. All subfigures indicate an empirical distribution within the sub-Rayleigh regime. 200kHz(a) refers to data collected during the 11 Mar 19 experiment, 200kHz(b) refers to data collected during the 12 Mar 19 experiment.

Figure 33. Probability of False Alarm: Plume Centre

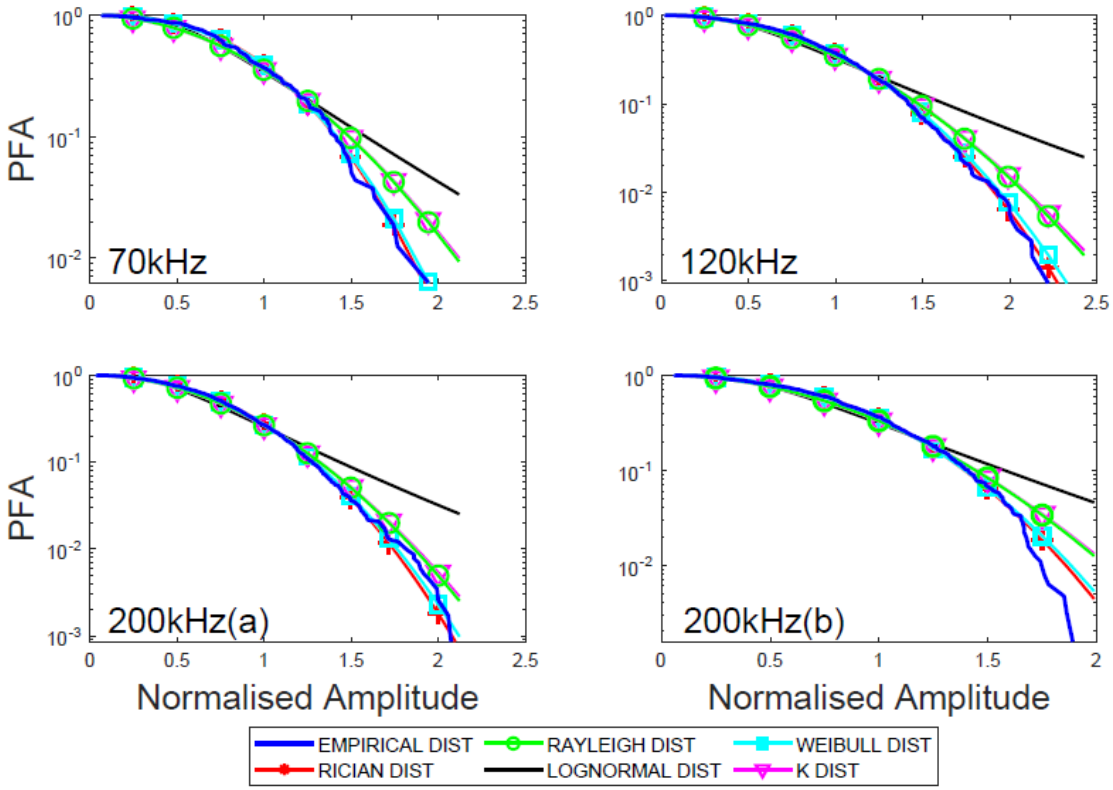

PFA vs Normalized Amplitude for the shear layer far zone. All subfigures indicate an empirical distribution within the sub-Rayleigh regime. 200kHz(a) refers to data collected during the 11 Mar 19 experiment, 200kHz(b) refers to data collected during the 12 Mar 19 experiment.

Figure 34. Probability of False Alarm: Shear Layer Far

The non-Rayleigh nature of the empirical distributions can be observed in the tails of all the plotted distributions. Note that all empirical distributions lie in the sub-Rayleigh regime, with the high amplitude echo returns having a lower PFA than that modeled by the Rayleigh distribution. The parameters used to construct the model distributions are tabulated in Table 6.

Table 6. PDF Parameters

Frequency	Zone	Rayleigh (λ)	Weibull (α,β)	K (α,ν)	Rician (ν,σ)	Lognormal (μ,σ)
70kHz	SLN	0.829	1.153,2.436	100,0.008	0.697,0.414	-0.277,0.460
	PC	0.939	1.067,1.989	33.337,0.282	0.340,0.641	-0.322,0.621
	SLF	0.933	0.975,2.748	100,0.009	0.790,0.393	-0.207,0.481
120kHz	SLN	0.839	1.156,2.229	100,0.008	0.665,0.445	-0.317,0.567
	PC	0.962	1.033,2.029	100,0.010	0.475,0.607	-0.303,0.632
	SLF	0.944	1.015,2.275	100,0.009	0.693,0.482	-0.266,0.588
200kHz(a)	SLN	0.740	1.336,2.272	100,0.007	0.597,0.438	-0.381,0.557
	PC	0.926	1.058,2.130	100,0.009	0.590,0.537	-0.301,0.609
	SLF	0.752	1.316,2.210	100,0.008	0.581,0.455	-0.386,0.582
200kHz(b)	SLN	0.757	1.305,2.203	100,0.008	0.556,0.473	-0.378,0.559
	PC	0.951	1.025,2.149	100,0.009	0.593,0.547	-0.280,0.585
	SLF	0.901	1.064,2.321	100,0.009	0.689,0.462	-0.283,0.575

To assess the accuracy, or goodness of fit between the empirical distribution and the model distributions, the nonparametric Kolmogorov-Smirnoff (KS) test statistic was used. The KS test statistic q describes the maximum absolute difference between the theoretical distribution $F(x)$ and the empirical distribution formed from N data samples $E_N(x)$, where

$$q = \max\left|F(x) - E_N(x)\right|, \quad -\infty < x < \infty \tag{21}$$

The null hypothesis is that the empirical distribution is drawn from the theoretical distribution, so it follows that as $N \to \infty, E_N(x) \to F(x)$. For large N, a q value close to zero validates the null hypothesis, if the q value is greater than a predetermined threshold or significance value, then the null hypothesis must be rejected (Papoulis and Pillai 2002).

To provide a means of comparing the results of the KS test between the different distributions, the *p*-value has been calculated, where the *p*-value is the probability of observing a test statistic greater value than q under the null hypothesis. If the *p*-value is small then it is less likely that we will observe a more extreme value for q under the null hypothesis, as the *p*-value approaches one, it becomes more likely that the observed data

follows the theoretical distribution. The KS test *p*-values for each frequency and zone are shown in Table 7, with all *p*-values of significance (which we will define here as greater than 0.8) highlighted in bold.

Table 7. KS Test *p*-Values

Frequency	Zone	Rayleigh	Weibull	K	Rician	Lognormal
70kHz	SLN	0.39	**0.96**	0.39	**0.96**	0.65
	PC	**0.96**	**0.96**	**0.91**	**0.96**	0.65
	SLF	0.39	**0.91**	0.39	**0.96**	0.31
120kHz	SLN	0.04	0.64	0.03	**0.82**	0.00
	PC	**0.96**	**0.98**	**0.95**	**1.00**	0.00
	SLF	0.04	**0.96**	0.03	**1.00**	0.00
200kHz (11 Mar)	SLN	0.37	**0.91**	0.29	**0.98**	0.01
	PC	**0.86**	**0.91**	**0.80**	**0.98**	0.00
	SLF	0.10	**0.98**	0.07	**1.00**	0.00
200kHz (12 Mar)	SLN	0.66	**0.80**	0.61	**0.88**	0.09
	PC	**0.91**	**0.96**	**0.88**	**0.94**	0.11
	SLF	0.07	**0.94**	0.06	**0.99**	0.00

It is acknowledged that use of model distribution parameters derived from the empirical data, strictly speaking, render Kolmogorov's theorem invalid (Fisz 1978). Even so, the *p* value is still widely used in this manner as it provides a reasonable measure of the goodness of fit between the empirical data and the model distributions (Lyons and Abraham 1999). Of note is that Rician distributions shows significant results for all datasets and the Weibull distribution all but one dataset. The Rayleigh and K distributions also showing a significant result for all PC zones.

THIS PAGE INTENTIONALLY LEFT BLANK

V. DISCUSSION

In the results section the following important observations were made; the scintillation is slightly less than unity, suggesting that a Rayleigh distribution may not be the best fit for the data; the KS test *p*-values indicate that the Rician and Weibull distributions are of best fit to the empirical data; and, that the Rayleigh and K distributions begin to show a significant goodness of fit within the plume center zone, i.e., the most turbulent zone of the plume.

We hypothesize that the characteristic structure of the thermal plume is responsible for separating the signal into two components. That is, there are large scale fluctuations associated with the weak temperature stratification of the water column, and the resultant change in density and mean sound speed (Table 3), which result in the coherent echo return. Also, that there are small scale fluctuations associated with the entrainment of the surrounding environment by the plume and turbulent mixing within the plume resulting in the relatively stronger sound speed variations, and an incoherent echo return. The two probability distributions that best fit the data (Weibull and Rician) are both related to physical scattering mechanisms via the Rayleigh distribution, however only one of the distributions provides an adequate physical explanation to our observations. If we return to our description of the Rician distribution (Ch II.D.4), it was noted that this distribution was designed to model a fixed signal in the presence of noise, which in this case can be considered as the coherent component and incoherent component respectively. By using Equation 17, with the derived parameters as listed in Table 6, we can estimate the strength of the coherent and incoherent components, we will refer to this quantity as the coherent to incoherent ratio (CIR) or, just as the dB difference between the two signals. The CIR is outlined in Table 8.

Table 8. Ratio of Coherent to Incoherent Echo Strength

Frequency	**Zone**		
	SLN (CIR, dB)	PC (CIR, dB)	SLF (CIR, dB)
70kHz	1.414, 3.0	0.141, -17.0	2.026, 6.1
120kHz	1.114, 0.9	0.306, -10.3	1.034, 0.3
200kHz (a)	0.929, -0.6	0.604, -4.4	0.816, -1.8
200kHz (b)	0.689, -3.2	0.586, -4.6	1.114, 0.9

Ratio of coherent to incoherent echo component. 200kHz(a) refers to data collected during the 11 Mar 19 experiment, 200kHz(b) refers to data collected during the 12 Mar 19 experiment.

As seen in Table 8, the coherent component appears to be of greatest relative value in the shear layer zones and decreases within the plume itself; this is consistent with our hypothesis. From our model of the thermal plume/free jet (ChII.A) the shear layers are the sharp boundary between the quiescent environment and the turbulent plume, this is where we would expect to see the greatest temperature differential as the cold water plume spreads out into the surrounding water. Since we have hypothesized that our coherent component is due to temperature stratification, it is therefore reasonable to link the observed increase in CIR with the presence of the temperature stratification across the shear layer. Transitioning into the plume center, there is a decrease in the CIR. That is, the incoherent component of the signal is becoming more significant. From the temperature experiment (ChIII.C.2) we found that the greatest turbulent activity was within the plume center. From our model of the thermal plume/free jet, it is expected that temperature stratification is weakest within the plume as the turbulent processes will result in the plume center being well mixed. Therefore, it is again consistent with our hypothesis that we see this reduction in the CIR at the plume center zone as temperature stratification is at its weakest (i.e., coherent component is small) and the turbulent processes are significant (i.e., incoherent component is large). As the CIR approaches zero the incoherent component dominates

such that Rician distribution approaches the Rayleigh distribution (Stanton et al. 2018), if we compare the CIR results to the KS-test *p*-values in Tables 7 we notice that the Rayleigh *p*-values become significant within the plume center.

Table 8 also eludes to a frequency dependence in the CIR. It appears that as frequency increases, we see less change in the CIR through the plume, and a less well defined boundary between the shear layers and the plume center. This is expanded on in Figure 35, where a linear fit has been overlaid on the CIR vs frequency plot. It is apparent that there is a power law decrease with frequency of the CIR through the shear layers, and a similar increase through the plume center. The parameters of these linear trends are outlined Table 9. We were unable to further expand on this result as we were unable to estimate the expected incoherent signal strength or identify at which subrange of the energy cascade peak backscattering had occurred. In doing so it would have allowed us to better gauge which physical dissipation mechanism was being observed and how this affects backscattering characteristics. In order to achieve this, we were required to measure or calculate the energy spectra out to the Bragg wavenumbers for each of the observed frequencies. From here we could compare the observed backscatter strength to a predicted backscatter strength via the techniques described by Goodman (1990) and Lavery et al. (2003).

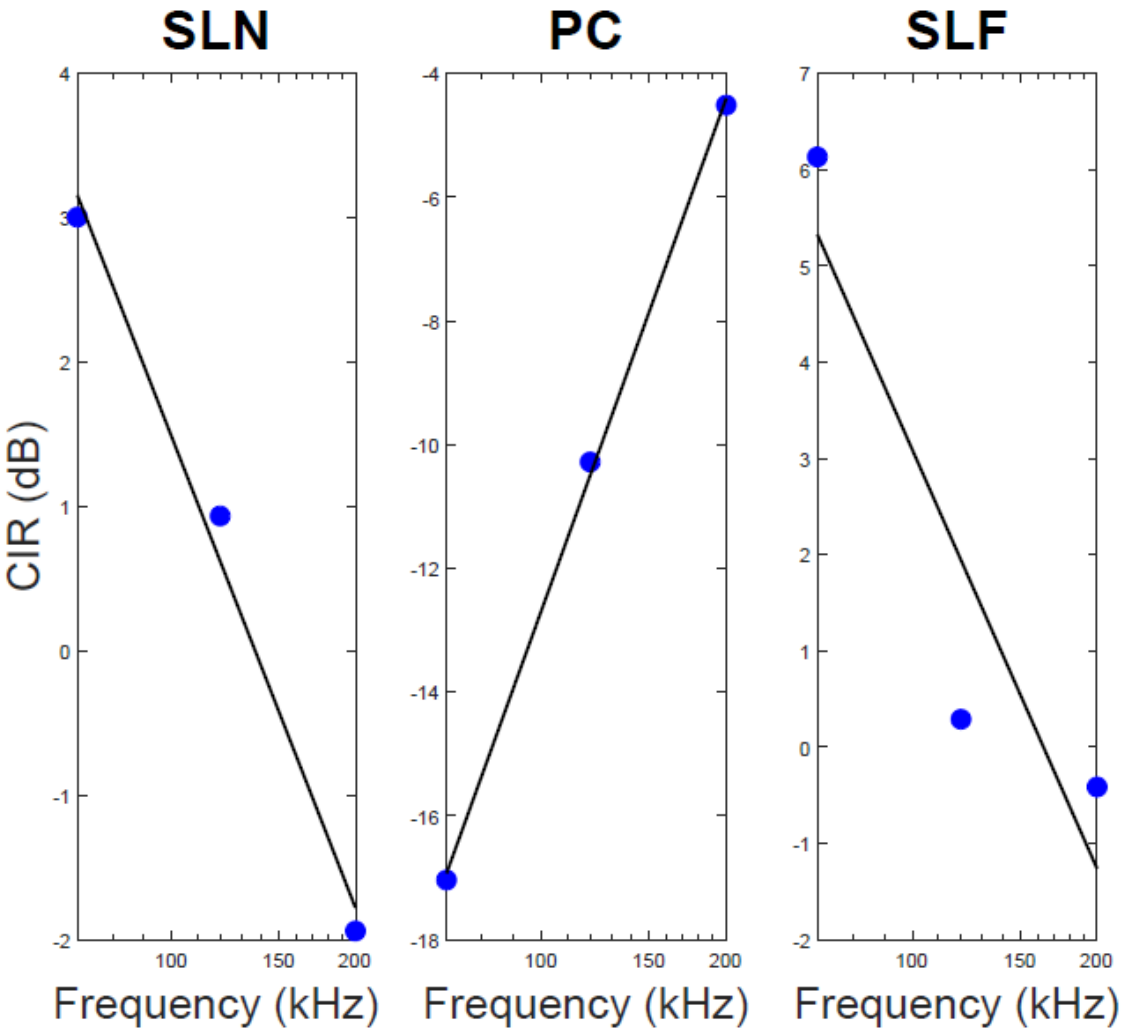

Coherent to Incoherent Ratio (CIR) in dB plotted against frequency on a log scale. A linear fit shows power law decay for both shear zones and power law growth for the plume center. The 200kHz results have been averaged into a single datapoint for each zone.

Figure 35. CIR vs Frequency

Table 9. CIR vs Frequency Trend Line Parameters

Zone	**Gradient**	**Intercept**
SLN	-10.8	23.1
PC	27.5	-67.6
SLF	-14.4	32.0

Figures 32 through 34 display a significant tapering off of the probability of false alarm (PFA) at the higher normalized amplitudes when compared with the Rayleigh distribution. This sub-Rayleigh behavior implies a lower false detection rate could be expected for target detection systems assuming Rayleigh statistics with a predetermined probability of false alarm.

THIS PAGE INTENTIONALLY LEFT BLANK

VI. CONCLUSION

In this thesis we have examined the statistics of high-frequency, narrowband echo-sounder backscatter through a negatively buoyant thermal plume. Data was collected using 70kHz, 120kHz and 200kHz transducers, focusing on the behavior of the backscatter as the acoustic waves passed through the turbulent plume, in particular, the entry, center and exit regions of the plume. It was found that the backscatter statistics are non-Rayleigh distributed.

The Weibull and Rician probability distributions provided the best fit to the observed data, where the Rician distribution also provided an adequate explanation of the physical mechanisms at play. That is, that the acoustic backscatter from the thermal plume can be considered as the coherent sum of two components; a coherent echo return component due to large scale fluctuations associated with the weak vertical temperature stratification of the water column; and, an incoherent echo return component due to small scale fluctuations associated with the turbulent mixing of the plume.

The results from the experiment have been displayed as probabilities of false alarm and compared against the Rayleigh distribution to illustrate the smaller tail of the empirical data and the matching Rician distribution. The implication of these results for undersea target detection is that echo backscatter due to a turbulent plume is unlikely to result in an increase false detection rate for systems assuming Rayleigh statistics with a predetermined probability of false alarm.

THIS PAGE INTENTIONALLY LEFT BLANK

LIST OF REFERENCES

Abdel-Rahman, A., 2010: A review of effects of initial and boundary conditions on turbulent jets. *WSEAS Transactions on Fluid Mechanics*, **4**, 257–275.

Abraham, D.A., and A.P. Lyons 2002: Novel physical interpretations of K-distributed reverberation. *IEEE Journal of Oceanic Engineering,* **27**, 800–813.

Ainslie, M.A., 2010: *Principles of Sonar Performance Modeling,* Springer, 707.

Ball, C.G., H. Fellouah, and A. Pollard, 2012: The flow field in turbulent round free jets, *Progress in Aerospace Sciences*, **50**, 1–26.

Biosonics, 2014: DT-X User Guide. Biosonics Inc, 33 pp.

Burdic, W.S., 1991: *Underwater Acoustic Systems Analysis (second edition),* Prentice Hall, 466 pp.

Chotiros, N.P., H. Boehme, T.G. Goldsberry, S.P. Pitt, A.L. Garcia, and R.A. Altenburg, 1986: Acoustic backscattering at low grazing angles from the ocean bottom. II. Statistical characterization of the bottom backscatter at a shallow water site. *J. Acoust. Soc. Am*, **77**, 975–982.

Colosi, J.A. 2016: *Sound Propagation through the Stochastic Ocean*. Cambridge University Press, 424 pp.

de Moustier, C, 1986: Beyond bathymetry: Mapping acoustic backscattering from the deep seafloor with Sea Beam. *Journal of the Acoust. Soc. Am*, **79** 316–331.

Fialkowski, J.M., and R.C. Gauss, 2010: methods for identifying and controlling sonar clutter. *IEEE Journal of Oceanic Engineering,* **35**, 330–354.

Fisz, M., 1963: *Probability Theory and Mathematical Statistics (second edition)*,Wiley.

Flatté, S. M., 1983: Wave propagation through random media: Contributions from ocean acoustics. *Proc. IEEE*, 71, 1267–1294.

Gallaudet, T. C., and C. P. de Moustier, 2003: High-frequency volume and boundary acoustic backscatter fluctuations in shallow water. *J. Acoust. Soc. Am*., **114**, 707.

Ghandi, P.P., and S.A. Kassam, 1988: Analysis of CFAR processors in nonhomogeneous background. *IEEE Transactions on Aerospace and Electronic Systems,* **24,** 427**–**445

Gibbs, J A., 2016: LES of Turbulent Flows. Accessed December 20, 2018, http://gibbs.science/les/lectures/lecture_03.pdf

Goodman, L., 1990: Acoustic Scattering from Ocean Microstructure. *Journal of Geophysical Research*, **95**, 557–573.

Jakeman, E., 1980: On the statistics of K-distributed noise. *J. Phys. A: Math. Gen.,* **13** 31–48.

Koay, C. G., and P. J. Basser, 2006: Analytically exact correction scheme for signal extraction from noisy magnitude MR signals. *Journal of Magnetic Resonance*, **179**, 317.

Kolmogorov, A.N., 1941: The local structure of turbulence in incompressible viscous fluid for very large Reynolds numbers. *Proceedings of the USSR Academy of Sciences*, **30**, 299–303.

Kundu, P.K., I,M, Cohen, and D.R. Dowling, 2012: *Fluid mechanics (fifth edition)*, Academic Press, 891 pp.

Lavery, A.C., R.W. Schmitt, and T.K. Stanton 2003: High-frequency scattering from turbulent oceanic microstructure: The importance of density fluctuations. *J. Acoust. Soc. Am*., **114**, 2685–2697.

Lavery, A.C., and T. Ross, 2007: Acoustic scattering from double-diffusive microstructure. *J. Acoust. Soc. Am*., **122**, 1449.

Lavery, A.C., W.R. Geyer, and M.E. Scully, 2013: Broadband acoustic quantification of stratified turbulence. *Journal of the Acoustical Society of America,***134**, 40–54.

Lee, W.J., and T.K.Stanton, 2016: Statistics of broadband echoes: Application to acoustical estimates of numerical density of fish. *IEEE Journal of Oceanic Engineering,* **41**, 709–723

Lyons, A.P., and D.A. Abraham, 1999: Statistical characterization of high-frequency shallow water seafloor backscatter. *J. Acoust. Soc. Am*., **106**, 1307.

Nortek, 2018: Signature Operations 250/500/1000kHz, version 10. Nortek Manuals, 53 pp.

Nortek, 2019: Nortek Product Catalogue 2019. Nortek Group, 66 pp, https://www.nortekgroup.com/assets/documents/Nortek_Productcatalogue_2019_web.pdf.

Olson, D.R., A.P. Lyons, D.A. Abraham, and T.O. Sæbø, 2019: Scattering statistics of rock outcrops: Model-data comparisons and Bayesian inference using mixture distributions, *The Journal of the Acoustical Society of America*, **145**, 761–774.

Oeschger, J., and L. Goodman, 1996: Acoustic scattering from a thermally driven buoyant plume. *The Journal of the Acoustic Society of America*, **100**, 1451.

Pope, S. B., 2000: *Turbulent flows*. Cambridge, UK: Cambridge University Press, 771 pp.

Papoulis, A., and S. U. Pillai, 2002: *Probability, Random Variables and Stochastic Processes (4th edition)*. Tata McGraw-Hill, 850 pp.

Prasad, R.R., and K. R. Sreenivasan, 1990: Measurement and interpretation of fractal dimension of the scalar interface in turbulent flows. *Phys. Fluids A*, **2**, 792–807.

RBR, 2017: RBR Duet Datasheet. RBR Ltd, 2 pp, http://rbr-global.com/wp-content/uploads/2018/01/0005585revA-RBRduet3-T.D-datasheet.pdf.

Reynolds, O., 1883: An experimental investigation of the circumstances which determine whether the motion of water shall be direct or sinuous, and of the law of resistance in parallel channels. *Philosophical Transactions of the Royal Society*, **174**, 935–982

Ross, T., and R, Lueck, 2003: Sound scattering from oceanic turbulence. *Geophysical Research Letters*, **30**, 1344.

Stanic, S. and E.G. Kennedy, 1993: reverberation fluctuations from a smooth seafloor. *IEEE Journal of Oceanic Engineering,* **18**, 95–99.

Stanton, T. K., and C. S. Clay, 1986: Sonar echo statistics as a remote sensing tool: Volume and seafloor. *IEEE Journal of Oceanic Engineering*, **OE-11**, 79–96.

Stanton, T.K., and D. Chu, 2010: Non-Rayleigh echoes from resolved individuals and patches of resonant fish at 2–4 kHz. *IEEE Journal of Oceanic Engineering,* **35**, 152–162.

Stanton, T.K., D. Chu and D.B. Reeder, 2004: Non-rayleigh acoustic scattering characteristics of individual fish and zooplankton. *IEEE Journal of Oceanic Engineering*, **29**, 260–268.

Stanton, T.K., D. Chu, J.M. Gelb, G.L. Tipple, and K Baik, 2015: Interpreting echo statistics of three distinct clutter classes measured with a midfrequency active sonar: Accounting for number of scatterers, scattering statistics, and beampattern effects. *IEEE Journal of Oceanic Engineering*, **40**, 657–665.

Stanton, T. K., W. J. Lee, and K. Baik, 2018: Echo statistics associated with discrete scatterers: A tutorial on physics based methods. *J. Acoust. Soc. Am*., **144**, 3124.

Talley, L.D., G.L. Pickard, W.L Emery, and J.H. Swift, 2011: *Descriptive physical oceanography (sixth edition)*. Academic Press, 555 pp.

Taylor, G. I., 1938: The spectrum of turbulence. *Proc. R. Soc. London Ser. A*, **164**, 476.

Thorpe, S. A., 2007: *An introduction to ocean turbulence.* Cambridge University Press, 293 pp.

Turner, J.S., 1969: Buoyant plumes and thermals. *Annu. Rev. Fluid Mech.,* **1**, 29–44.

Urick, R. J., 2010: *Principles of underwater sound.* Peninsula Publishing, 423 pp.

Ward K.D., 1981: Compound representation of high resolution sea clutter. *Electron. Lett.*, **17**, 561–563.

INITIAL DISTRIBUTION LIST

1. Defense Technical Information Center
   Ft. Belvoir, Virginia

2. Dudley Knox Library
   Naval Postgraduate School
   Monterey, California